Development and implementation of computational approaches to quantify cell-generated mechanical forces

Nikita Kalashnikov

Department of Chemical Engineering

McGill University, Montreal

July 2020

A thesis submitted to McGill University in partial fulfillment of the requirements for the degree of Master of Engineering

Abstract

For a long time, cells have not been receiving the credit they deserve and have been treated only as 'the smallest building block of life'. They are not just passive inert materials, but rather are complex beings that can move around and generate as well as respond to forces within their small environment. Furthermore, they can also come together and combine their forces in order to form a stronger whole as a tissue. Advances in technology have recently enabled researchers to build realistic cellular microenvironments that stimulate cells to behave as they would in the body. However, it remains equally important to also develop the necessary tools to study their mechanical behavior in order to understand how and why they generate mechanical forces within these environments. In this thesis, I attempt to quantify the forces produced by cells and tissues by building controlled environments and using computational tools. First, I ran finite element simulations to model the tissue retraction process in an injured collagen microtissue and learned that wounding establishes a long-lasting significant hoop stress around the wound edge, which we believe promotes future closure of the tissue lesion. Second, I fabricated soft compliant polyacrylamide and collagen substrates, and modified an existing traction force microscopy procedure to measure traction stresses established by adherent single cells and multicellular colonies on these matrices. Using the synthetic substrates, I measured the forces created in placenta-derived BeWo cell colonies and hypothesized that the more defined stress profile established in the smaller colony promotes BeWo cell fusion into a syncytium. Traction forces of fibroblasts seeded on collagen gels with and without neutrophil extracellular traps were also estimated, and these results suggest that neutrophil extracellular traps bind to the collagen network, stiffen the matrix locally and drive increased force generation by the cells. Last, I developed the computational pipeline necessary to analyze the deformation of microspherical stress gauges (MSGs) and computed the stresses established within multicellular spheroids from experimental deformation data obtained by my colleagues. Using this pipeline, we determined that a thin layer of cells at the spheroid edge is kept under tension and drives outside-in contraction, producing the large compressive stresses maintained within the spheroids.

Résumé

Pendant longtemps, les cellules on était vue juste comme «les plus petits éléments constitutif du vivant». Cependant, elles ne sont pas seulement des matériaux inertes passifs, mais plutôt des êtres complexes qui peuvent se déplacer et générer ainsi que répondre aux forces dans leur petit environnement. En outre, ils peuvent également se rassembler et combiner leurs forces afin de former un tout plus fort en tant que tissu. Les progrès technologiques ont récemment permis aux chercheurs de créer des micro-environnements cellulaires réalistes qui stimulent les cellules à se comporter comme elles le feraient dans le corps. Cependant, il reste tout aussi important de développer également les outils nécessaires pour étudier leur comportement mécanique afin de comprendre comment et pourquoi ils génèrent des forces mécaniques dans ces environnements. Dans cette thèse, j'essaie de quantifier les forces produites par les cellules et les tissus en construisant des environnements précis et en utilisant des outils computationnels. Tout d'abord, j'ai effectué des simulations par la méthode des éléments finis pour modéliser le processus de rétraction tissulaire dans un microtissu de collagène blessé et j'ai appris que la blessure établit une tension tangentielle importante et durable à l'entour de la plaie circulaire, ce qui, selon nous, favorise la fermeture future de la lésion tissulaire. Deuxièmement, j'ai fabriqué des substrats de polyacrylamide et de collagène souples, et j'ai modifié une procédure de microscopie de force de traction («*traction force microscopy*») existante afin de mesurer les forces établies par les cellules monocellulaires adhérentes et les colonies multicellulaires sur ces matrices. En utilisant les substrats synthétiques, j'ai mesuré les forces créées dans les colonies de cellules BeWo, dérives du placenta, et j'ai émis l'hypothèse que le profil de traction plus défini établi dans la petite colonie favorise la fusion des cellules BeWo en un syncytium. Les forces de traction des fibroblastes ensemencés sur des gels de collagène avec et sans filets de neutrophiles («*neutrophil extracellular traps*») ont aussi été estimées, et ces résultats suggèrent que les filets s'attachent au réseau de collagène, le rigidifient localement et pousse les cellules à générer des forces plus élevées. Enfin, j'ai développé la procédure de calcul nécessaire pour analyser la déformation des jauges mécaniques microsphériques et calculé les forces établies au sein des sphéroïdes multicellulaires à partir des données de déformation expérimentales obtenues par mes collègues. Nous avons déterminé qu'une fine couche de cellules au bord des sphéroïdes est maintenue sous tension et cause une contraction qui oppose les forces de compression maintenues à l'intérieur des sphéroïdes.

Acknowledgments

The time I spent conducting research in the CMED lab under the guidance of Prof. Christopher Moraes and the impact it had on me is far beyond what is reflected in this thesis. I was a shy and reserved undergraduate student, who would sometimes eat in class instead of taking notes, when Prof. Moraes saw something in me and accepted me into his lab. It would be an oversight to say that my research experiences did not change me.

I would like to extend my greatest thanks to you, Chris, for playing a massive part in making me who I am today. You were never really my supervisor (well, maybe, only until I got used to calling you Chris) and always treated me more as a colleague and a friend rather than as a student. I will aspire to do the same in my own career. Your unwavering enthusiasm along with your creative, yet rational, approach to science and engineering has sparked in me an interest in scientific investigation and exploration that I hope to keep and cultivate for the rest of my life. It would be unfair to list out everything you have done for me here, but I would like to thank you for all the opportunities you gave me. But, most importantly, you assembled an amazing group of people that conducts extraordinary research and I feel privileged to be a part of it. No wonder I stayed to complete a Master's degree.

Our lab is simply wonderful. Everyone brings in a little bit of themselves, creating a unique fun, positive and supportive lab atmosphere that lets research flourish. Sarah, I am so grateful that we joined the lab at the same time and that it lead to our friendship. You know me better than most and I am so glad that you are somehow able to drag me out into the wild with you! Thank you Steph for coming up with crazy activities to do, Ray for supporting her and helping implement them, and Wontae for looking after us. I will never forget our first trip to the mountain. Thank you all for creating the foundation for this lab! Sanya, I miss our deep philosophical discussions about life, but am glad that I inherited your desk spot. Being a part of the fun office, I witnessed its magic and saw how it was able to bring the whole lab together better than the conference room ever did.

Over the past four years, I got the chance to meet so many great people. Thank you: Arvind for getting me to learn COMSOL; Camille for relating to my passion for medicine; Carley for your unique perspective on life; Christina for our late night lab chats; Gabe for asking the right questions; Karthick for the 4th floor lab; Lisa for teaching me 3D printing; Nick for your sarcasm

and seeing you on the 6th floor at random times; Sonya for your sense of humor; and Zhenwei for being my badminton partner. I also want to thank the undergrads who were there with me or came after me for bringing their own little spark to our lab events: Patty, Xavier, Chalani, Rachel, Vickie, Erica, Pooja, Anqi, Emily and Chen. To the students I helped in a supervisory capacity over the years, Stephanie and Lidan, I hope I helped you discover what research really is. Thank you for I have learnt more from you than you might think. For everyone that is starting out in our lab: you are in for a great time, enjoy it while it lasts!

I am also very grateful for having the opportunity to collaborate with some amazing labs throughout the years. Thank you Meghan from the Spicer lab and Tobias from the Harrington lab for your advice and thoughts on my projects. Meghan, I really enjoyed travelling to the hospital for the neutrophils; and, Tobias, I don't think I will ever forget your 'Xbox controller' microscope.

Outside of the lab, I would like to thank my friends, Michel and Marco, for tolerating me when I could not stop talking about research. Thank you to my ambulance friends for the jokes and laughter that distracted me when I did not want to talk about research.

I don't know exactly when you will read this, Mom. Thank you for always wanting to know how my experiments went, but really for everything you do for me. Thank Dad for me.

Overview of contributions

Even though this thesis was written by the author in its entirety, the work that made it possible is a result of a highly collaborative effort that was under the guidance of Dr. Christopher Moraes. All finite element simulations and experiments described in the methods and results sections were completed by the author. Unless otherwise stated below, data collection and analysis was also performed by the author.

In Chapter 2, I describe how I built a wounding model *in silico* from experimental wound retraction data and literature cell-laden collagen gel material characterization data. I use this model to perform a viscoplastic stress analysis and highlight the creation of a long-lasting significant hoop stress around the wound edge. The evolution of mechanical stresses over time after tissue injury predicted by the model formed the basis for the hypothesis that active wounding mechanically promotes future closure. The experimental wound characterization data was collected by Sarah Dubois, who also built the wounding system. Both as co-first authors, we published this combined work in *Tissue Engineering C* in 2019.

In Chapter 3, I validate a modified version of an existing polyacrylamide gel traction force microscopy procedure with the HS-5 fibroblast model cell line, and then apply it to study the stress patterns formed by BeWo cell clusters grown on polyacrylamide gels and to estimate the traction forces of single cells grown on soft collagen gel substrates with and without embedded neutrophil extracellular traps. Prabu Karthick Parameshwar built the patterned polyacrylamide substrates on which he cultured BeWo cells to form colonies. We obtained the relaxed and stressed fluorescent images as well as the bright field images together and then I independently completed the traction force analysis. This experiment was included in a work published in *ACS Applied Materials & Interfaces* in 2019. Separately, I fabricated leukocyte-loaded collagen gels that I stimulated to produce neutrophil extracellular traps for traction force microscopy. The polymorphonuclear leukocytes used were obtained from Meghan de Meo. Collagen gel Raman spectroscopy and associated spectrum analysis was performed in collaboration with Tobias Priemel. This work is expected to be submitted for publication in the next year.

In Chapter 4, I build a model to relate microspherical stress gauge (MSG) deformation to applied stresses and use it to develop a computational pipeline that makes it possible to analyze

stresses produced within 3D multicellular tissues. Wontae Lee fabricated the microspherical stress gauges, embedded them in multicellular spheroids and measured the deformation of the sensors. I used my computational pipeline to process all of the sensor deformation data and highlight the specific stress pattern formed within the spheroids. Wontae Lee also completed the mechanical characterization experiments and I only built the model that relates the osmotic pressure tests on the hydrogel sensors to rheological findings from large gels. Wontae Lee compiled, analyzed and interpreted all of the data depicted in Figure 15 and Figure 18. Combined with multiple other experiments performed by our numerous collaborators, we published this work in *Nature Communications* in 2019.

Table of contents

List of figures

List of tables

Chapter 1: Introduction

1.1 Motivation

Cell biology has long been focused on uncovering the chemical basis of cell behavior, yet cells are inherently active mechanical entities that crawl around and generate mechanical forces and respond to various mechanical loads within their microenvironment (1–4). In fact, cells have an internal organization or structure in the form of a cytoskeleton that ultimately determines their mechanical properties and functional capabilities. It is by altering their cytoskeleton that cells can satisfy functional needs of adhesion, proliferation, differentiation and migration (5). In addition, on a larger scale, cells can come together, form colonies or larger tissues, and then mechanically act in a coordinated fashion essentially as one complete construct (6–8). Thorough examination into cell and tissue mechanics only really began in the last decade thanks to the advent of enabling technologies that allow for the fabrication of realistic cellular microenvironments and that make it possible to measure as well as to manipulate mechanical forces present in these environments (9–13). The increasing scientific interest in the contribution of mechanics to biology gave rise to two distinct, yet very related, research fields: cell biomechanics and mechanobiology (14).

Cell biomechanics focuses on characterizing the intrinsic mechanical properties of cells and understanding how cells mechanically interact with their environment. Cell mechanical behavior is quite complex since it arises from the collective state of the cytoskeleton rather than from a single structural component (15). As a result, cell biomechanics looks at how global structural changes within the cytoskeleton drive cellular mechanical processes, may they be desirable for the cell in the context of physiology or even undesirable in various pathological conditions. Since the cytoskeleton is inherently complex and its whole condition cannot be captured from single proteins, cell mechanical properties, which are intimately linked to the cytoskeleton, provide a means to assess the state of the cell and even forecast future cell behavior (16). As a result, cellular mechanical properties such as stiffness can be used as measures of cell phenotype and can even be used as integrative mechanical biomarkers of disease (17).

Mechanobiology, on the other hand, looks at the biological response of cells to various external mechanical conditions (18). Ever since the discovery of the first *in vitro* cell line, life science research has been conducted on hard plastic Petri dishes and it is only now that researchers

are starting to realize that the environment in which cells are cultured in has a profound impact on their behavior. This realization is directly tied to the field of mechanobiology, which really aims to understand how various mechanical aspects of the environment shape cell behavior and determine cell fate (19). To this end, at the core of mechanobiology is the design of novel cellular microenvironments that provide specific mechanical cues to cells by replicating the body's normal as well as diseased environments. As a result, mechanobiology does not only bring new fundamental insight into complex mechanical phenomena that occurs in the body, but it also provides more faithful platforms for drug discovery as well as novel mechanical stimulation approaches for tissue engineering (20).

Investigating the mechanical nature of cells and tissues can be thought of as a two-step process where, first, cells are seeded into a carefully designed environment that stimulates them to behave mechanically, and then a thorough analysis is performed to extract valuable mechanical information from the observed cell behavior. Not surprisingly, this endeavor presents itself with significant engineering challenges. Not only must the cellular microenvironment be engineered to resemble the native environment of the human body in order to accurately replicate cell behavior *in vitro*, but the environment must also allow control over experimental conditions and parameters in a way that facilitates the subsequent mechanical analysis. Microfabrication techniques combined with designer biomaterials make it possible to create complex biomimetic platforms to study cell behavior at a scale relevant to cells and at a high throughput. However, the more complex the system is the more difficult it is to decipher and analyze the mechanical activity of the cells within it as they interact with their environment. Therefore, there is a need to adapt existing and develop new strategies to evaluate the mechanical forces at play in these more advanced systems.

1.2 Thesis overview

The overall goal of the work presented in this thesis is to examine how cellular mechanical activity can be analyzed computationally in three distinct systems: (i) wound retraction in a microtissue wounding platform, (ii) traction forces on flexible soft substrates produced by single fibroblast cells and BeWo cell colonies, and (iii) mechanical stress patterns within multicellular spheroid tissues using deformable sensors. Hence, the thesis is organized accordingly with a chapter dedicated to each system and with a final conclusion at the end.

Chapter 2:
Modelling wound retraction computationally

2.1 Background

Finite element modelling (FEM) is an established numerical method that is used to solve problems in engineering and physics when an analytical solution is difficult or even impossible to obtain. The strength of this method comes from discretization. By dividing the geometry of interest into smaller units or finite elements, the multiple partial differential equations that describe the overall behavior of the system simplify into more manageable algebraic equations. With enough computational power, these algebraic equations can be solved for each finite element and combined to yield an overall solution to the problem at hand. As it turns out, finite element modelling finds many uses since most practical problems either have complicated geometries, a multitude of loading conditions or evolving material properties. Perhaps, the most obvious application of modelling is for designing and prototyping. By creating models and testing them *in silico*, scientists and researchers can bypass resource-intensive steps of prototyping and proof-of-concept tests, and thereby quickly come up with the most optimal design.

Finite element modelling does not necessarily have to solve an optimization problem or guide a design: it can also be used to analyze a system and try to understand what drives its behavior. With the increasing influence of engineering in the biological sciences, finite element analysis is finding new opportunities (21–23). Modelling the behavior of biological systems is challenging, but can give insight into how each element of the system contributes to its global behavior, and – in the process – it can help generate novel hypotheses and push research forward (24).

Traumatic injury to a soft tissue and the tissue's subsequent response with wound closure is a particularly interesting biological phenomenon (25) that is difficult to replicate accurately *in vitro*. Nevertheless, we developed an inexpensive and easy-to-use microtissue wounding platform that makes it possible to monitor wound dynamics after tissue injury (26). Collagen fibroblast microtissues can be formed between four pillars and then, after the tissue contracts and forms a

pre-stressed tissue, a 3D-printed wounding construct can be used to guide a needle to wound the tissue in a precise location as illustrated in Figure 1.

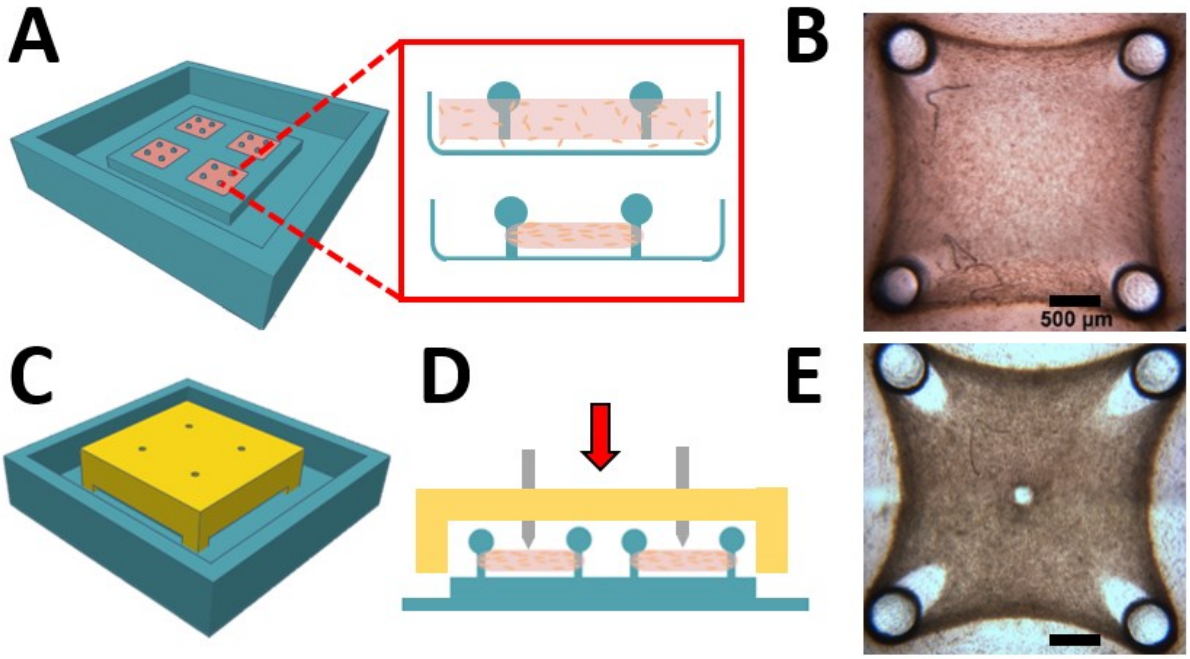

Figure 1. Overview of the engineered tissue wounding platform. (A) Schematic overview of the tissue culture device in operation. Cell laden collagen is loaded into silicone wells containing replica-molded 3D-printed anchoring pillars, which then contracts to form a pre-stressed tissue suspended between the pillars. (B) Representative bright field image of pre-stressed tissue. (C) Schematic overview of the wounding device in operation. A 3D printed structure with integrated needles is designed to fit over positioning grooves in the culture substrate, precisely locating the needles at defined locations over the engineered tissues. (D) Manually pressing the wounding platform down creates (E) well-defined and precisely positioned holes in the collagen tissues (reused from (26) with permission from Mary Ann Liebert, Inc. publishers).

Using this platform, we were readily able to observe the characteristic elements of the wound healing process: wound formation, retraction and closure (Figure 2). In particular, we noticed that, when the tissue is actively punctured, it retracted significantly upon injury and then closed up quickly in a day (Figure 2A). In comparison, when an object or an obstruction was passively removed from the tissue, it did not retract and only left a void in the tissue that did not close over the span of two days (Figure 2B). We hypothesized that active injury to the tissue causes mechanical stresses to build up around the wound perimeter, activating cells to contract and facilitating subsequent wound closure. To estimate these potential stresses, in this section, I build a collagen microtissue material model and simulate the active wounding process computationally.

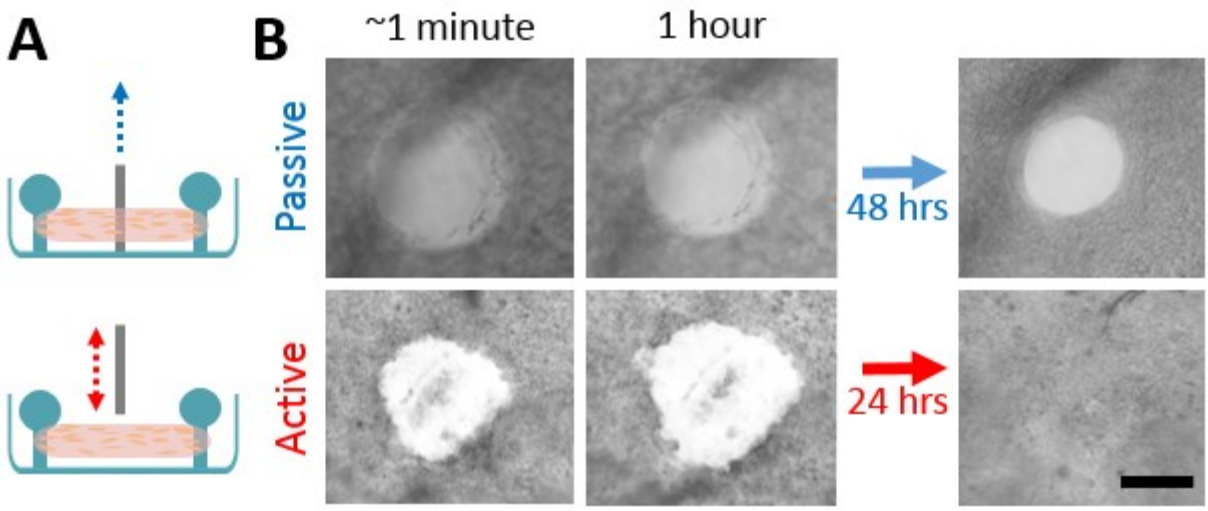

Figure 2. Direct comparison between passive and active wounding. (A) Tissues were either passively wounded by removing an obstruction from the tissue or actively wounded with the 3D printed wounding device to achieve small wounds. (B) Passively formed wounds partially closed within 48 hours, but actively formed wounds first expanded and then closed completely within 24 hours (scale bar = 250 μm) (adapted from (26) with permission from Mary Ann Liebert, Inc. publishers).

2.2 Finite element analysis methodology

Traditionally, the finite element method follows a straightforward procedure where the type of analysis is specified, and the model geometry is built and then assigned material properties. Once the model is fully defined with boundary conditions such as forces, displacements or stresses, it can be solved for the primary field variable, which – for mechanics problems – is typically displacement, and then additional variables such as stress and strain can be estimated from the displacement field.

2.2.1 Inverse finite element modelling strategy

Direct mechanical characterization approaches are extremely challenging given the present system. Not only are the mechanical properties of cell-contracted collagen gels complex, but they are evolving over time due to wounding-associated cell-driven matrix remodeling (27). Along with temporal variations in material properties, the structure of the microtissue varies spatially with denser regions closer to the pillars. Considering these significant limitations and the associated difficulties in implementing the traditional FEM procedure, I utilized an inverse finite element approach and implemented it in COMSOL (Burlington, MA, USA). By first initializing the material properties with formulations and parameters from literature sources for cell-laden collagen hydrogel mechanical characterization (28–31) and then tuning them iteratively within a

reasonable range to match experimental observations, it was possible to develop a working model of the microtissue wounding process *in silico*. Previous efforts in modelling collagen materials computationally included linear elastic, viscoelastic and viscoplastic material models. The parameter-tuned material formulation that best matched the areal wound increase of about 40% in approximately 20 minutes (Figure 3B) was selected to evaluate the stresses that develop within the microtissue.

2.2.2 Material formulations

The deformation observed in a tissue and the mechanical forces associated with it are related to each other through the tissue's mechanical properties. In other words, material properties relate the tissue stresses to its strains and various material formulations exist to describe this relationship. Biological tissues are inherently complex materials and, with an applied stress or strain, exhibit a behavior that is a combination of multiple distinct mechanical responses, including – but not limited to – elasticity, viscoelasticity and plasticity. Linear elastic models were implemented with a simple elastic modulus E_{e} (28), which is represented as a spring in the spring/dashpot circuit system in Figure 3C. Viscoelasticity was introduced by adding a spring-dashpot Maxwell arm, characterized by an instantaneous elastic modulus E_{v} and a viscosity μ, in parallel to the elastic branch (29). Viscoplastic behavior was modelled with a series addition of another viscosity term η with a yield stress σ_{Y} threshold coupled to a linear softening function $\sigma_{\mathrm{Y}}(H)$. The latter reduces the yield stress under constant loading. Mathematically, a linear Norton-Hoff model was used to describe viscoplasticity, relating viscoplastic strain $\varepsilon_{\mathrm{vp}}$ to stress σ_{vp}:

$$\frac{\mathrm{d}\varepsilon_{\mathrm{vp}}}{\mathrm{d}t} = A\sigma_{\mathrm{vp}}^{n} = \frac{1}{\mu}\sigma_{\mathrm{vp}}$$

where the exponent n is set to 1, following the perfect viscoplastic assumption, and the rate coefficient A to be the inverse of the viscosity μ (28).

The material parameters taken from the relevant literature and the ranges tested are presented below along with the final values obtained from the iterative inverse finite element approach.

Table 1. Collagen microtissue material formulations and parameters.

Reference	Parameter	Literature values	Range tested	Final value (Figure 3D)
Linear elastic				
Raub et al., 2007 (32)	Elastic modulus (E_e)	1-10 kPa	0.01-100 kPa	5.1 kPa
Viscoelastic				
Feng et al., 2010 (29)	Elastic modulus (E_e)	5.1 kPa	0.01-100 kPa	5.1 kPa
	Instantaneous elastic modulus (E_v)	4.5 kPa	0.5-50 kPa	4.5 kPa
	Viscosity (μ)	143.6 kPa·s	10-1000 kPa·s	143.6 kPa·s
Viscoplastic				
Malandrino et al, 2019 (28)	Yield stress (σ_Y)	0.3 kPa	0.1-5 kPa	1 kPa
	Hardening slope (H)	$-2/3$	$-2/3$	$-2/3$
	Viscoplastic dashpot viscosity (η)	100 kPa·s	10-1000 kPa·s	574 kPa·s

2.2.3 Geometry

From experimental observations, it was clear that the wounding process generates a local wound that minimally affects the overall tissue dimensions. This implies that changes in wound size do not translates to the tissue edges and that the model geometry only has to capture the central tissue region (Figure 3B). As a result, the tissue regions around the four pillars can be neglected and this drastically simplifies the necessary simulations in terms of geometry as well as material properties. In particular, the latter change closer to the tissue edges since those are much denser. Hence, a simple 2D axisymmetric geometry of radius 750 μm and thickness of 1 mm, as observed under a microscope, with homogeneous material properties was implemented to model the tissue. In addition, a central 'hole' region was included in the model in which the material properties are set to zero to initiate the wounding process.

2.2.4 Boundary conditions

There are no explicitly defined forces or strains acting on the boundaries of the model since the simulated injury occurs within the model domain. However, the collagen tissue contracts over time as a result of cell-mediated matrix remodeling and, as a result, a certain level of pre-stress is

established within it since it is anchored to the four pillars. To include this into our model, we quantified the degree of tissue pull-away from the pillars and determined it to be equivalent to a 33% radial strain, which was set as a boundary condition in the model.

2.2.5 Model meshing

The model was initially discretized very finely with 2 μm quad elements near the hole domain where the strains and stresses are expected to be highest. To reduce model computational requirements, we conducted a mesh size sensitivity analysis and increased the mesh size throughout the tissue domain. No significant changes in computed strains and stresses were observed and a mapped quad element size set to 1% of the total microtissue length was ultimately selected. This ensured a coefficient of variation of less than 1% and the mesh element quality was above 0.9 during the simulations.

2.3 Results

2.3.1 Modelling wound expansion to match experimental observations

In vitro wounding experiments revealed that wounds, irrespective of their original size, grow in size for approximately 20 minutes until stabilizing at 1.4 times their initial size (Figure 3B). Using this information and the iterative inverse finite element method, we tested our parameter-tuned linear, viscoelastic and viscoplastic model materials in order to determine which model better recapitulates the observed tissue behavior in response to wounding. Not surprisingly, the linear elastic model did not exhibit any time-dependent behavior and, instead, the wound instantaneously grew to its final size to release all of the tissue pre-stress. A viscoelastic model did introduce a time-dependent element into the model (Figure 3D), but it was not sufficient enough to recapitulate the large wound expansion magnitude observed experimentally (Figure 3B).

Along with local observations of wound closure, the wounding experiments also revealed the extent of cell-associated collagen remodeling as can be observed along the tissue edges in Figure 1E. The edges appear denser and there is significant tissue pull-away from the anchoring pillars when compared to Figure 1B. Cells are, in fact, causing permanent changes in the structure of their collagen matrix by pulling on it, which causes some crosslinks to break and new ones to be formed. The concept of irreversible structural changes is typically described as plasticity, which

can be modelled quite easily. In this case, these permanent changes evolve over time and this suggests that a time-dependent plasticity model should capture this behavior. Thankfully, collagen tissue viscoplasticity has been explored in recent studies (28,31,33–35). Implementing this material model (Figure 3C) made it possible to accurately replicate experimentally-observed wound retraction *in silico* both in terms of magnitude and time dynamics while using material parameters (Table 1) reasonably similar to those obtained from cell-laden collagen gel mechanical characterization studies (Figure 3D).

2.3.2 Evolution of stress patterns during wound retraction

After finding the most appropriate material formulation for our model, we ran simulations to see how the stresses within the tissue evolve over time after wounding (Figure 3E). Wounding causes an immediate decrease in radial stress from the baseline stress value of about 2 kPa that continues to decrease over time as the wound gets bigger due to viscoplasticity (Figure 3F). The hoop stress or the stress established in the circumferential direction along the edge of the wound evolves in a more dramatic fashion. It increases immediately along the edge of the wound and this increase gets less significant over time as the wound perimeter gets bigger; however, a transient stress peak is established deeper into the tissue (Figure 3F). Even though tissue viscoplasticity causes stress to dissipate over time, the elevated hoop stress visible in a thin band around the wound, but not immediately next to it, is still significant for over one hour (Figure 3E).

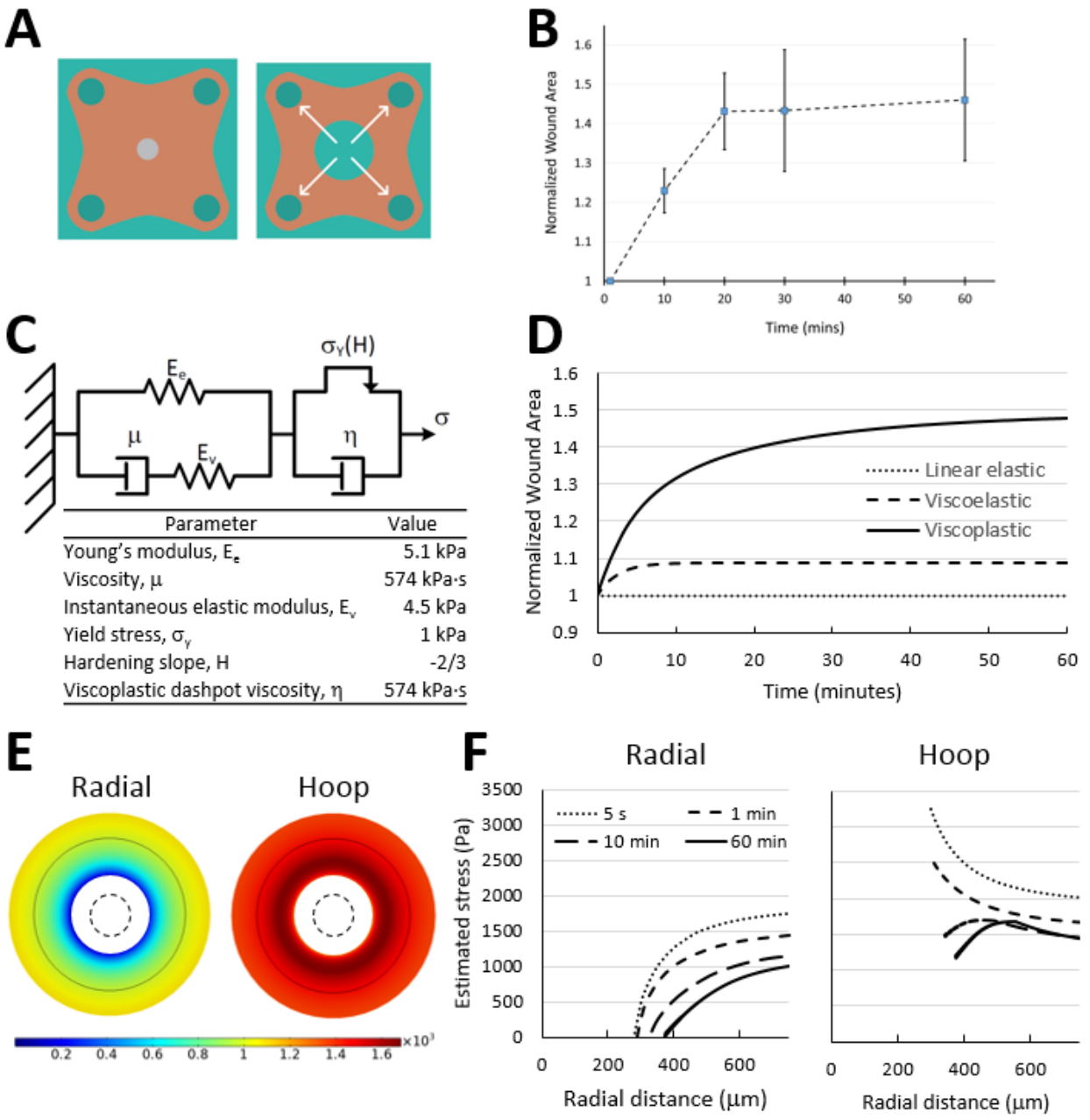

Figure 3. Wound retraction following tissue puncture and corresponding finite element model. Overview of wound expansion. (B) Temporal evolution of wound area normalized to initial wound size after tissue puncture. Wounds appear to grow for 20 minutes until they reach a steady-state size that is 50% bigger than the initial wound area. (C) Complete material network implemented for the finite element analysis of wound retraction and associated parameter values used in the simulations. The material model features a viscoelastic component with parameters μ and E_v as well as a viscoplastic dashpot element that is activated when the tissue deforms past its yield point, defined by σ_Y and η. A linear hardening function with a negative slope H is used to account for tissue softening, characteristic of cell-laden collagen tissues past their yield stress. (D) Simulated wound retraction for simple linear elastic, viscoelastic and full material models. Time-dependent wound retraction is present with both viscoelastic and viscoplastic models, but only the latter reaches the experimentally observed expanded wound sizes. (E) Characteristic radial and hoop stresses established after complete wound retraction with dashed lines indicating the initial wound size immediately after tissue puncture. (F) Spatial radial and hoop stress profiles within the tissues at steady-state. Wounding causes a reduction in radial stress near the wound edge and a corresponding transient increase in hoop stress. Viscoplastic stress dissipation works over time to attenuate both stress profiles, leaving a characteristic hoop stress peak near the wound, but not immediately adjacent to it (reused from (26) with permission from Mary Ann Liebert, Inc. publishers).

2.4 Discussion and impact

The finite element analysis conducted here does present with some significant limitations. The material parameters are taken from literature and have not been directly obtained from mechanical characterization tests, which means that the absolute tissue stresses estimated by the models are likely to be inaccurate. However, the stress patterns that are formed within the tissue remain valid and the results can be consider accurate by considering the calculated stress values as relative and not as absolute. Furthermore, the mechanical properties in the area around the wound are considered homogenous. This is highly unlikely given the extent to which the wound expands. Since wounding does not affect the overall shape of the tissue, wound retraction most definitely causes cells to compact near the wound edge and creates a densified region near the wound as can be observed in Figure 1E. Finally, even though wounds produced using this platform are relatively circular (Figure 2B) and a more accurate geometry would not give significantly different results in our model, wound shape plays an important role in wound closure since it can alter the surrounding stress field (36) and is correlated with wound healing (37).

Nevertheless, these simulations indicate that a circumferential hoop stress is created around a wound and persist for a long time. Since cells contract when subjected to stress gradients (38) and there is evidence that wound closure occurs through an actin purse-string based mechanism with elevated hoop stresses at the wound edge (39), these results suggest that the transient hoop stresses created during viscoplastic tissue retraction might be responsible for mechanically activating cells to contract, migrate and close the gap in the tissue, thereby contributing to wound closure.

The modelling results presented here provide insight into the wound retraction process and propose that the mechanical properties of the injured tissue direct future wound closure. In conjunction with additional *in vitro* experiments, this work establishes a basis for future studies into the mechanobiology of wounding, which has profound implications in the fields of tissue repair and regeneration.

Chapter 3:
Quantifying cell traction forces on soft substrates using a modified traction force microscopy procedure

3.1 Background

Although finite element modelling is a powerful tool that makes it possible to analyze how mechanical forces arise in biological systems such as tissues, it cannot be used to accurately quantify these forces without rigorous mechanical testing necessary to obtain specific modelling parameters. Since characterizing the mechanical properties of living cells and tissues comes with significant challenges, a different approach would be to place cells in a controlled mechanically-defined environment and then to infer the mechanical forces present in the system from interactions between the cells and this artificial environment. Hence, carefully designed cell culture platforms with controlled experimental conditions can help in quantifying cell-generated forces more accurately and bypass the limitations of simulating biological behavior using finite element analysis. Taking inspiration from the field of mechanobiology, biomaterials and fabrication techniques necessary to create these environments can be implemented to achieve this goal (9,12,20).

Hydrogels are becoming a standard biomaterial that is used in tissue engineering and mechanobiology research (40). They can be either synthetic or natural, but they are all made out of a cross-linked network of polymer chains that is highly hydrophilic, attracting and containing significant amounts of water. Even if hydrogels consist of about 90% water, the hydrogel's cross-links cannot be dissolved and, as a result, they retain their solid structure and integrity (41).

Used in standard wet biology laboratories for gel electrophoresis, polyacrylamide (PAA) is one of the first hydrogels implemented for research in mechanobiology. It is a highly inert synthetic biomaterial with which cells cannot interact with; however, its surface can easily be functionalized through its carboxylate groups to allow cells to attach and spread. In addition, it is highly linearly elastic with a modulus that can be tuned easily by adjusting the monomer to cross-linker ratios (42). These characteristics make polyacrylamide an ideal controlled 'blank slate' material.

However, since they are synthetic, polyacrylamide gels do not always best mimic the native environment within the body. As an alternative to polyacrylamide, gels formed by cross-linking collagen fibers prove to recapitulate the *in vivo* microenvironment much better (43). Collagen gels are natural hydrogel that are much more biocompatible in that cells can, not only attach and spread, but can also invade into them and remodel them. This also means that they are more difficult to characterize mechanically and, in general, these hydrogel tend to be much softer and have non-linear mechanical properties.

Both of these hydrogels have been at the forefront of biomaterial research and have been successfully used for cell biomechanics and mechanobiology research. That being said, protocols have been developed to make these gels, functionalize them if necessary and bind them to various surfaces. In addition, although collagen's mechanical properties are more complex, both hydrogels are amenable to mechanical characterization and are excellent candidates to produce platforms for cell force measurements. In fact, these hydrogels can be made soft enough that, when cells spread on them, they actively pull on the surface and generate cell traction forces (44,45). These forces have been shown to play key roles in physiological (46–49) and pathological processes (50,51). Cells such as fibroblasts that participate in the wound healing process tend to have more significant traction forces, owing to their extracellular matrix remodeling requirements (52). On the other hand, metastatic cancer cells displays larger traction forces, which has been established as a potential mechanical biomarker of disease (53).

Cell traction forces can quantified by obtaining the displacement field surrounding an adherent cell as it pulls the surface in various direction and displaces small fiducial fluorescent markers embedded in the biomaterial substrate. Computationally, this displacement field can then be converted to the corresponding stress field to reveal the desired traction forces produced by the adherent cells (54–58). In this section, I develop traction force microscopy (TFM) capabilities for both polyacrylamide and collagen substrates, and then apply them to (i) compute traction forces in placental trophoblast-derived BeWo cell clusters and (ii) estimate fibroblast traction stresses seeded on collagen gels with and without embedded neutrophil extracellular traps (NETs).

3.2 Materials and methods

Unless otherwise stated, all chemical were purchased from Sigma-Aldrich (Oakville, ON) and all cell culture materials from Fischer Scientific (Ottawa, ON). All data was compiled and analyzed in EXCEL.

3.2.1 Polyacrylamide gel fabrication and functionalization

Flat coverslip-bound polyacrylamide (PAA) traction force substrates can easily be fabricated by casting the polyacrylamide solution with fluorescent beads prepared beforehand between a silanized coverslip and a hydrophobic glass slide, and letting it sit for the free-radical polymerization reaction to occur. The gel stays bound to the coverslip and the whole construct can be carefully removed from the glass slide. After washing the hydrogels extensively to remove the remnant cytotoxic precursor PAA components, the free surface of the gel can be functionalized with collagen to allow cell attachment and spreading (59).

Glass coverslips were treated with a solution of 0.4% (v/v) 3-(Trimethoxysilyl)propyl methacrylate in acetone by immersion for 5 minutes, washed in acetone for another 5 minutes and left to dry. Large glass slides were made hydrophobic using a Rain-X spray solution. The polyacrylamide solution was prepared according to recipes presented in detail elsewhere (42). Briefly, the precursor polyacrylamide solutions were prepared by mixing acrylamide (Bio-rad, 1610140) with bis-acrylamide (Bio-rad, 1610141) to achieve a desired final ratio (Table 2) in phosphate buffered saline (PBS). In addition, 0.5% by volume of 0.5 μm diameter carboxylate-modified fluorescent beads (FluoSpheres, Invitrogen) were introduced into the solution. To polymerize 450 μL of the polyacrylamide base solution, 50 μL of 1% (w/v) ammonium persulfate (APS; Bio-rad, 1610700) initiator in PBS was added to the solution along with 0.75 μL of tetramethylethylenediamine (TEMED) catalyst. Then, 25 μL droplets of the overall mixture were deposited onto the hydrophobic slide and a coverslip was placed over each one of the droplets. All components were filter sterilized prior to use.

Table 2. Polyacrylamide hydrogel formulations.

Nominal stiffness (kPa)	**1.2**	**2.4**	**3.9**
Acrylamide (wt%)	3	7.5	4
Bisacrylamide (wt%)	0.1	0.03	0.3

After leaving enough time for gelation to occur, each gel was detached from the glass slide, placed into an appropriate well plate and washed with sterile PBS three times for 5 minutes each on a shaker. The gels were then sterilized under a UV germicidal lamp for an hour and left in a solution of 1% (v/v) anti-anti in PBS, sealed with parafilm, overnight in the fridge for swelling to occur. To functionalize the substrate for cell culture, the polyacrylamide surface was washed, placed over droplets of a 0.1 mg/mL Sulfo-SANPHA (G-Biosciences, BC38) in PBS solution on a parafilm-covered surface of a Petri dish and exposed to UV for 4 minutes. This process was repeated one more time. Then, the hydrogels were placed over droplets of a 0.1 mg/mL collagen I (Advanced BioMatrix, #5005) in PBS solution and left overnight in a parafilm-sealed Petri dish in the fridge until cell seeding. All functionalization steps were performed in a biological safety cabinet (BSC).

3.2.2 Collagen gel fabrication

Using a similar 'sandwich' approach, a neutralized collagen solution can be gelled in an incubator between a functionalized and a non-functionalized glass coverslip (60). The gel can then be released from one of the coverslips, left in media to swell overnight and can be seeded with cells.

To allow collagen to bond to one of the glass coverslips during gelation, half of the coverslips were first silanized using a 2% (v/v) (3-aminopropyl)triethoxysilane acetone solution by immersion for 15 minutes at room temperature in a fumehood. After washing the coverslips in pure acetone for 5 minutes and air drying them for 15 minutes, they were placed into a 0.1% (v/v) glutaraldehyde RO water solution for 15 minutes to complete the functionalization. These coverslips were then placed into a well plate and washed extensively on a shaker with RO water for 5 minutes three times. To prepare 300 μL the collagen gel precursor solution, 20 μL of 10X Dulbecco's modified Eagle's medium (DMEM) was titrated with 1M sodium hydroxide (NaOH), which changed from yellow to bright pink at the titration endpoint. Then, sterile water was added to achieve a total volume of 40 μL. Typically, about 1.5 μL of NaOH were necessary to complete the titration, which led to the following recipe (Table 3).

Table 3. Collagen hydrogel recipe.

Component	Volume (μL)
10X DMEM	20
1M sodium hydroxide (NaOH)	~1.5
Sterile water	~18.5
7.5% sodium bicarbonate (NaHCO3) buffer	10
1X DMEM	50
3 mg/mL bovine collagen type I	150
Cell suspension or 1X DMEM	48.5
0.5 μm diameter carboxylate-modified fluorescent beads	1.5
Final 1.5 mg/mL collagen gel volume	300

According to it, the remaining components were added sequentially to produce the final 1.5 mg/mL precursor collagen gel solution. Then, 100 μL droplets of the mixture were placed onto the non-functionalized glass coverslips, covered with the functionalized ones and placed in an incubator for approximately 30 minutes to reach complete gelation. When the gels turned slightly more opaque and enough time has passed, a small amount of media was deposited near the hydrogel to detach it from one of the coverslip through capillary action. The coverslip-bound collagen traction force substrates were then recovered and placed into a well plate filled with media for swelling to occur and until further use. To ensure sterility, the collagen solutions were prepared and casted inside of a BSC.

3.2.3 Rheology

The polyacrylamide hydrogels have been previously well characterized mechanically (61), but the collagen gels have not. To determine the mechanical properties of these gels, rheological tests were performed using a Discovery HR-2 rheometer (TA instruments). To secure the collagen gel samples on the rheometer, packaging tape was applied on the bottom plate and superglue was used to glue the glass-side of the sample to the tape. The top plate was then lowered until enough contact was achieved. The bottom plate temperature was also set to 37ºC. Amplitude sweeps at a frequency of 1 Hz with a strain ranging from 0.01% to 1% were completed to obtain the storage (G') and loss moduli (G") of the gels, following established collagen characterization protocols (62–64).

3.2.4 Cell culture

Human bone marrow fibroblasts (HS-5; ATCC) were used as the model cell line when developing the traction force systems. These cells were grown in Dulbecco's modified Eagle's medium (DMEM; Gibco) supplemented with 10% fetal bovine serum (FBS) and 1% antibiotic-antimycotic (AA) at 37^{o}C and 5% CO_2. Trypsin was used to harvest the cells for passaging into a new T-flask or for cell seeding onto the traction force substrates.

Polyacrylamide hydrogels micropatterned with adhesive fibronectin patches, produced following an established protocol (65), and seeded with placenta-derived trophoblast-like BeWo cells were provided to me by my colleague. Separately, polymorphonuclear leukocytes (PMNs) – which mostly consist of neutrophils – were obtained from a collaborator, added to the precursor collagen gel solution and, after collagen gelation, activated with 2μM phorbol 12-myristate 13-acetate (PMA) for 3 hours to produce neutrophil extracellular traps (NETs).

3.2.5 Traction force microscopy procedure

After seeding the traction force substrates and leaving them overnight in the incubator for the cells to attach and spread, the gels were rinsed with PBS and transferred into a coverslip chamber (Chamlide CMB, Quorum Technologies; Puslinch, ON, CA). 500 μL of media was added and the chamber was placed into a circular microscope stage insert (Ibidi GmbH; Gräfelfing, Germany). To prevent the formation of salt crystals due to the PBS, the bottom of the coverslip was gently wiped with an ethanol-soaked wipe.

Once the sample was secured on the microscope stage, a spinning disc confocal microscope (Olympus IX-73) with a sCMOS Flash 4.0 camera was used to obtain an image of the stressed state of the uppermost fluorescent bead layer along with a phase contrast image in each region of interest. To obtain the reference or stress-free image of the beads, the cells were killed either using a 1% (w/v) sodium dodecyl sulphate (SDS) PBS solution or a 0.1% (v/v) Triton-X PBS solution, depending on the substrate. SDS breaks down the plasma membrane of the cells and solubilizes proteins very efficiently in less than a minute after addition, which makes it the best choice for a killing agent. Unfortunately, it also degrades collagen to some extent and causes the gel to go out of focus on the microscope. As a result, SDS was used for the polyacrylamide TFM substrates,

whereas a milder membrane-lysing agent, Triton-X, was implement for the cell-laden collagen gels.

The reference and stressed bead images were compiled into a stack in ImageJ, aligned to account for experimental drift using a template alignment plugin and analyzed using a particle velocimetry (PIV) plugin to determine the bead displacement field, following previous protocols (66). The bead displacements were estimated following an iterative PIV procedure where, with each iteration, the interrogation window was made smaller. The final displacement field grid was selected to have about 3-5 beads per interrogation window. To remove erroneous displacement vectors, a dynamic mean test for low correlation values was performed. This test removed the outlier values and replaced them with an average displacement calculated from the neighboring interrogation windows. After obtaining the final displacement field data, traction force fields were reconstructed using a custom MATLAB code, which solves the inverse Boussinesq problem using the Fourier space solution – following the Fourier transform traction cytometry (FTTC) method (67) – and produces the displacement and force plots.

The Young's modulus or stiffness value used for the traction force calculations in the simple collagen gel condition was obtained from rheological data and corresponded to 126 Pa. On the other hand, due to unexpected circumstances out of our control, we were unable to mechanically characterize the collagen-NETs gels. Following some previous preliminary observations (data not shown, collaborating labs), the stiffness of these gels was assumed to be double that of the pure collagen gels.

3.3 Results

3.3.1 Fibroblast traction forces on polyacrylamide substrates

After successfully producing polyacrylamide traction force substrates that have a good fluorescent bead coverage, we seeded human bone marrow HS-5 fibroblast cells, known to be mechanically active, on the surface of the gels to test whether we could estimate their traction forces. Most fibroblasts adopted an elongated morphology as highlighted in Figure 4A. Although the bead displacements were not visible by eye during the experiment, they became readily apparent after aligning the relaxed and stress images (Figure 4B). The subsequent computational

analysis revealed expected displacement fields (Figure 4C) and associated traction stress heat maps (Figure 4D) with higher displacements and stresses near the two ends of the elongated cells.

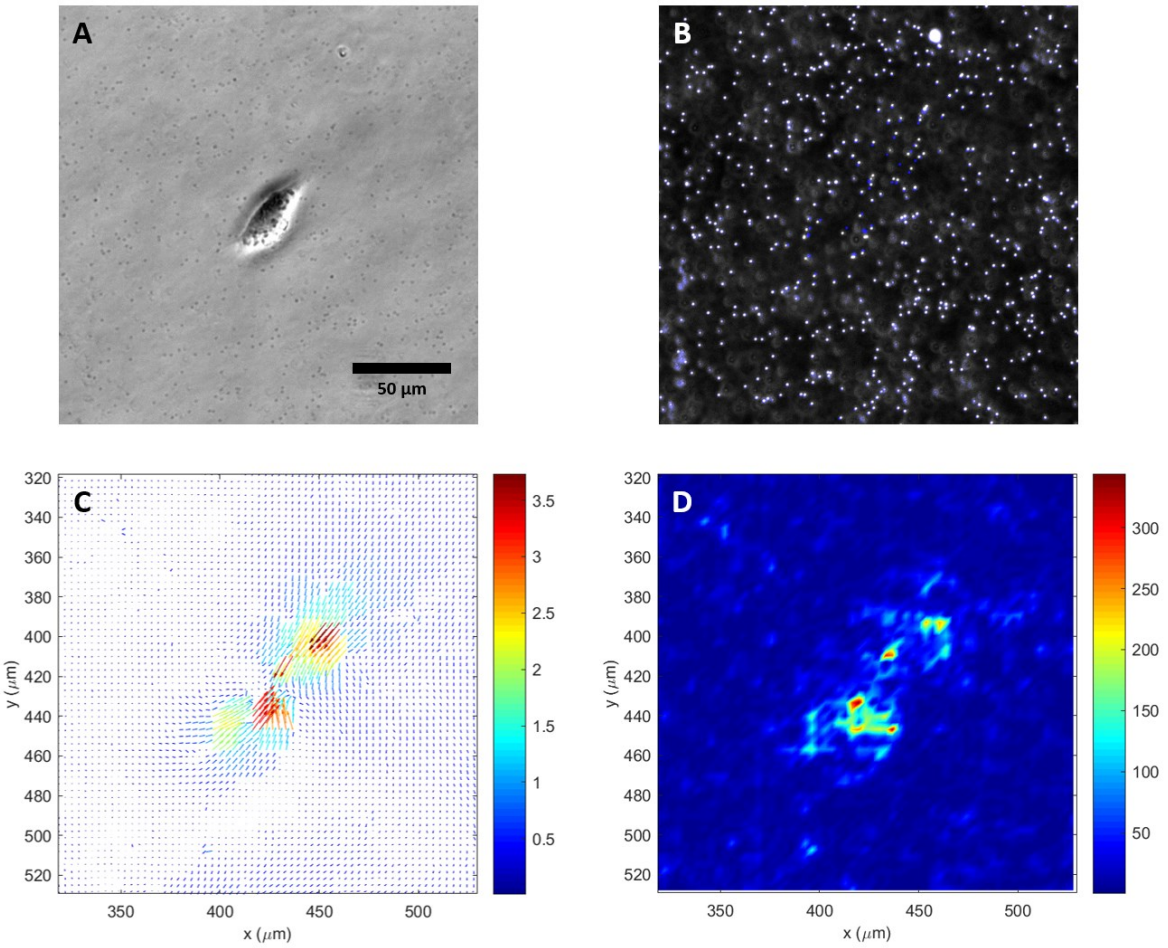

Figure 4. Representative cell traction force computation procedure. (A) Phase contrast image of a fibroblast cell on a polyacrylamide hydrogel. (B) Fluorescent confocal image stack (grey corresponds to the reference state obtained after cell detachment and blue indicates observed bead displacement). (C) PIV vector field (displacements in µm) and (D) traction force magnitude (traction stresses in Pascal units) plots.

To further validate our system, we conducted TFM experiments for HS-5 cells on both soft and stiff gels. Cells spread more and generate larger total traction stresses on the stiffer substrates, as their cell area is higher along with the sum of their traction forces (Figure 5A-B). Furthermore, when the traction stresses produced by the cells were normalized to their spread area, the fibroblasts on the stiffer gel still outperformed the ones grown on the softer variant (Figure 5C). This suggests that the stiffer matrix mechanically activates the cells to pull harder, which is consistent with the literature (68).

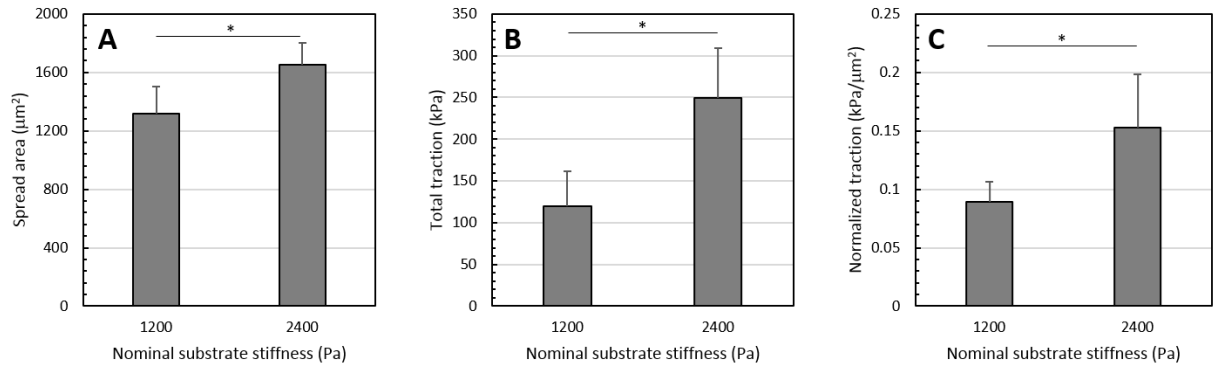

Figure 5. Fibroblast traction forces on polyacrylamide substrates. (A) Fibroblasts attach and spread more on stiffer substrates. In addition, stiffer substrates mechanically activate fibroblasts and result in significantly larger (B) total traction forces, even when (C) normalized to their spread area ($p<0.05$, $n=5$; data reported as mean +/- standard deviation).

3.3.2 Force patterns in placental trophoblast clusters

We produced polyacrylamide hydrogels patterned with fibronectin circular patches of various sizes using a microcontract printing protocol (65) and seeded BeWo cells on these gels. The BeWo cells formed small (~100 μm) and large (~400 μm) colonies on these adhesive patches (Figure 6A and Figure 7A) and undoubtedly generated forces on their substrates, which we aimed to quantify using our traction force computation procedure. From the displacement vector plots, a clear ring of high displacement can be qualitatively identified near the 100 μm colony edge (Figure 6B), but is not as apparent and seems to be more fragmented in the larger 400 μm colony (Figure 7B). In fact, bead displacements are more consistent around the edge of the small colony with small variations of 1 μm around a baseline value of 3 μm, as opposed to an average displacement of about 7 μm in the larger colony, but with 4 μm variations. Considering the traction stress magnitude plots, the forces around the edge do not produce a clear ring pattern and, instead, arise in small patches, lining the colony edge in the small cell cluster (Figure 6C). This is even more pronounced in the large cell colony (Figure 7C).

Using the symmetry inherent to these colonies, the Cartesian vector field images were transformed into polar counterparts in order to obtain the average displacement or stress along various lines passing through the colony. Averaging these linear profiles and plotting them against the normalized radial position within the cell colony gave us the displacement and stress profiles depicted in Figure 6D and Figure 7D.

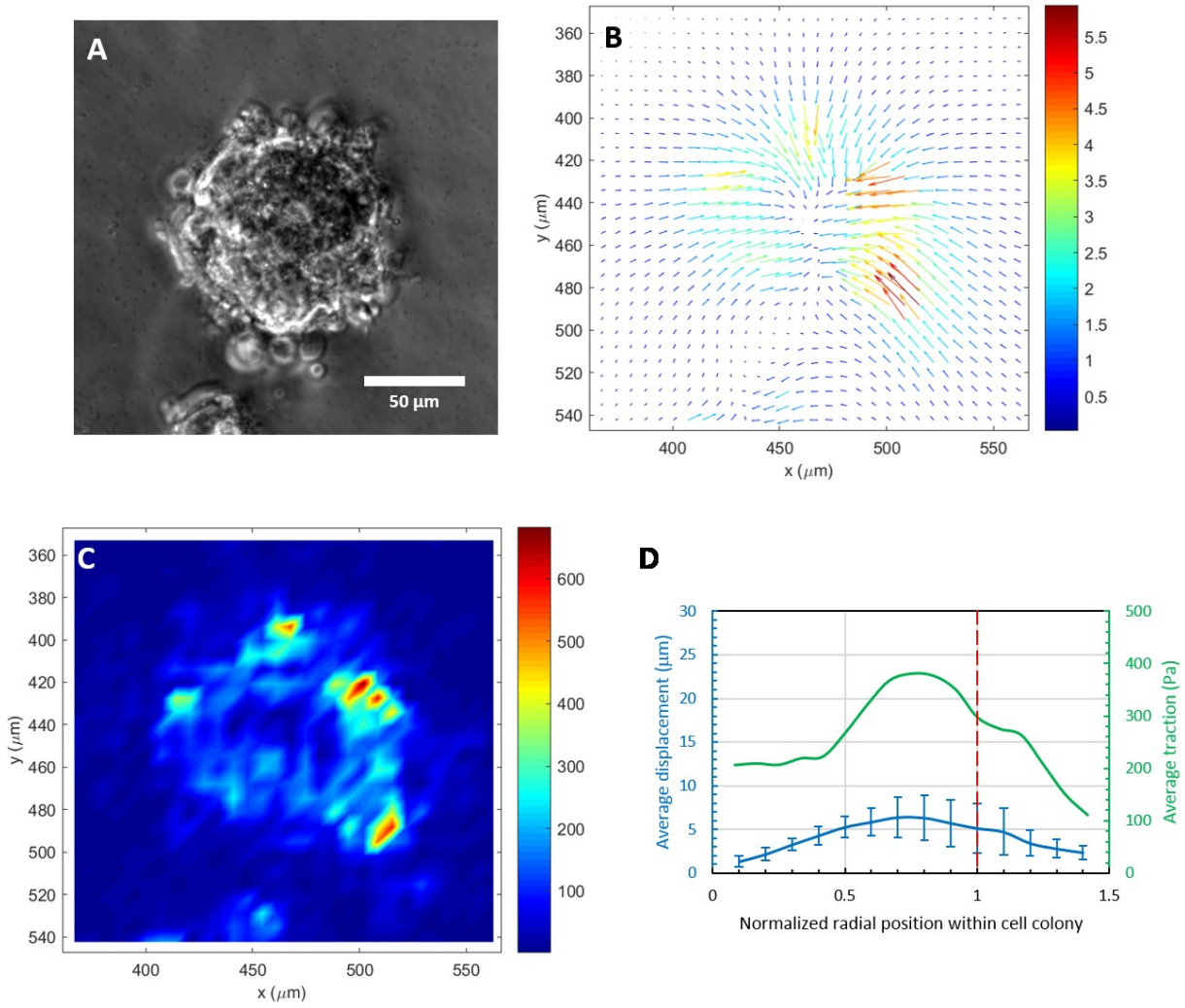

Figure 6. Traction forces within a small BeWo cell cluster. (A) Representative phase contrast image of a 100 µm BeWo cell colony grown on a fibronectin adhesive patch created on a polyacrylamide hydrogel along with corresponding (B) displacement field (displacements in µm and standard deviation for error bars) and (C) traction force magnitude (traction stresses in Pascal units) plots. (D) Average displacement and traction stress profile established across the cell colony highlights the prominent forces generated at the colony edge (as indicated by the dashed red line).

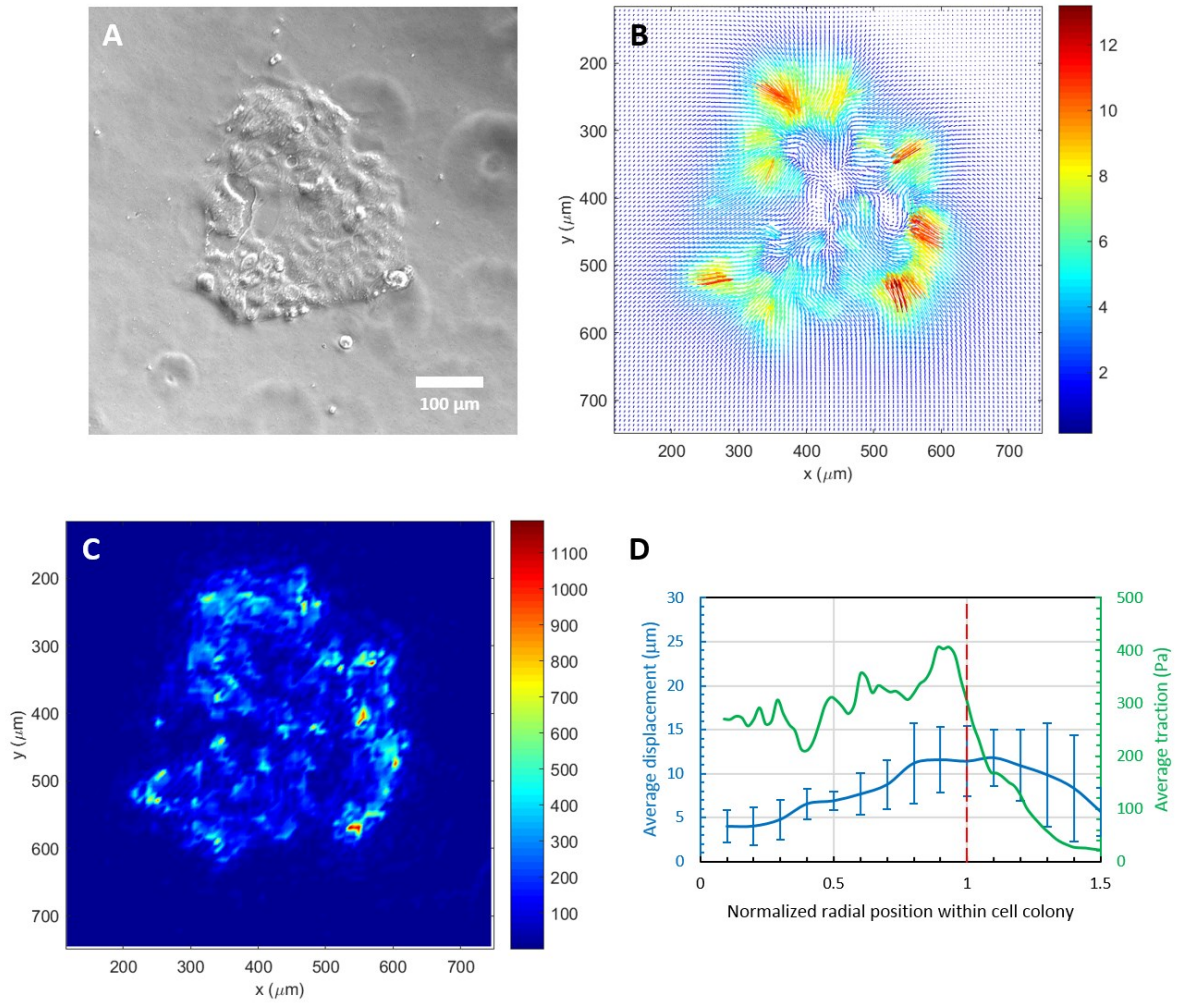

Figure 7. Traction forces within a large BeWo cell cluster. (A) Representative phase contrast image of a 400 µm BeWo cell colony grown on a fibronectin adhesive patch created on a polyacrylamide hydrogel along with corresponding (B) displacement field (displacements in µm with standard deviation for error bars) and (C) traction force magnitude (traction stresses in Pascal units) plots. (D) Average displacement and traction stress profile established across the cell colony highlights prominent heterogeneity in forces within the colony and a slight peak at the colony edge (as indicated by the dashed red line).

In both cases, the average traction stress appears to increase towards the colony edge and to decrease away from it. The smaller colony has a much more consistent profile with a baseline average traction of about 150 Pa within the colony (Figure 6D), whereas the stress within the larger colony is much more heterogeneous (Figure 7D), ranging from ~220 Pa up to ~350 Pa. Aside from the differences in baseline stress established within the colonies, the stress peaks are quite different between the two colony sizes. The stress within the smaller cell cluster transitions smoothly to a stress peak of about 260 Pa that seems to plateau and is maintained across almost half of the colony. In addition, this stress ramps down gradually away from the colony edge. In the larger colony, the stress spikes to ~400 Pa near the colony and is not nearly as broad as the stress plateau in the small

colony. Furthermore, as can also be observed qualitatively on the displacement field plots, the variance on the displacement measurements is much more significant and heterogeneous for the larger clusters.

The smaller cell cluster morphologically appears to be more balled up (Figure 6A) compared to the larger cluster where cells seem to spread much more (Figure 7A). It is reasonable to assume that the cells in the smaller colony have not attached well to the gel and instead prefer to bind to each other with only the edge cells holding the colony in place. This stronger cell-to-cell attachment could cause the cells to better coordinate and produce a more organized force profile. In the bigger colony, the cells spread out more and interact only with their closest neighbors, generating larger but more local stresses.

3.3.3 Mechanical properties of collagen gel traction force substrates

Compared to polyacrylamide hydrogels, collagen gels exhibit complex mechanical behavior that can cause some difficulties when attempting to run mechanical characterization tests on them. In particular, collagen gels are viscoelastic and undergo stress relaxation, which is an observed decrease in stress in response to an applied strain. In the context of rheology, when the rheometer top plate is lowered to the sample, this manifests itself with a detected positive normal force upon initial contact that is then rapidly lost due to a reduction in stress inherent to the gel.

In order to determine how stress relaxation could impact rheological findings, a gap distance sweep was performed, starting from initial contact until 150 μm deep into the gel (Figure 8A). Clearly, the moduli increase the more the top plate squeezes the gel, which could cause drastic inaccuracies, especially when the gap distance beyond initial contact is pushed past 100 μm. In addition, the measurement takes some time to stabilize near the initial point of contact. This brief experiment led to the conclusion that the plate must be lowered slightly below the initial point of contact, but not past 50 μm into the gel.

Using this procedure to establish an appropriate gap distance, multiple collagen gels were tested using an amplitude sweep (Figure 8B). From the moduli plots, it is clear that the measurement stabilizes in the initial steps and then slowly drops with increasing strain, which is most likely due to gel slipping at the wet top plate boundary. Aggregating the mechanical property data at about a strain of 0.17% where the properties seem to maintain for a brief period gives a

storage modulus of about 42 Pa (or an approximate Young's modulus of 126 Pa) and a loss modulus of 6 Pa for collagen gels (Figure 8C) with some variability, which can be attributed to the differences in gap distance settings or gelation dynamics.

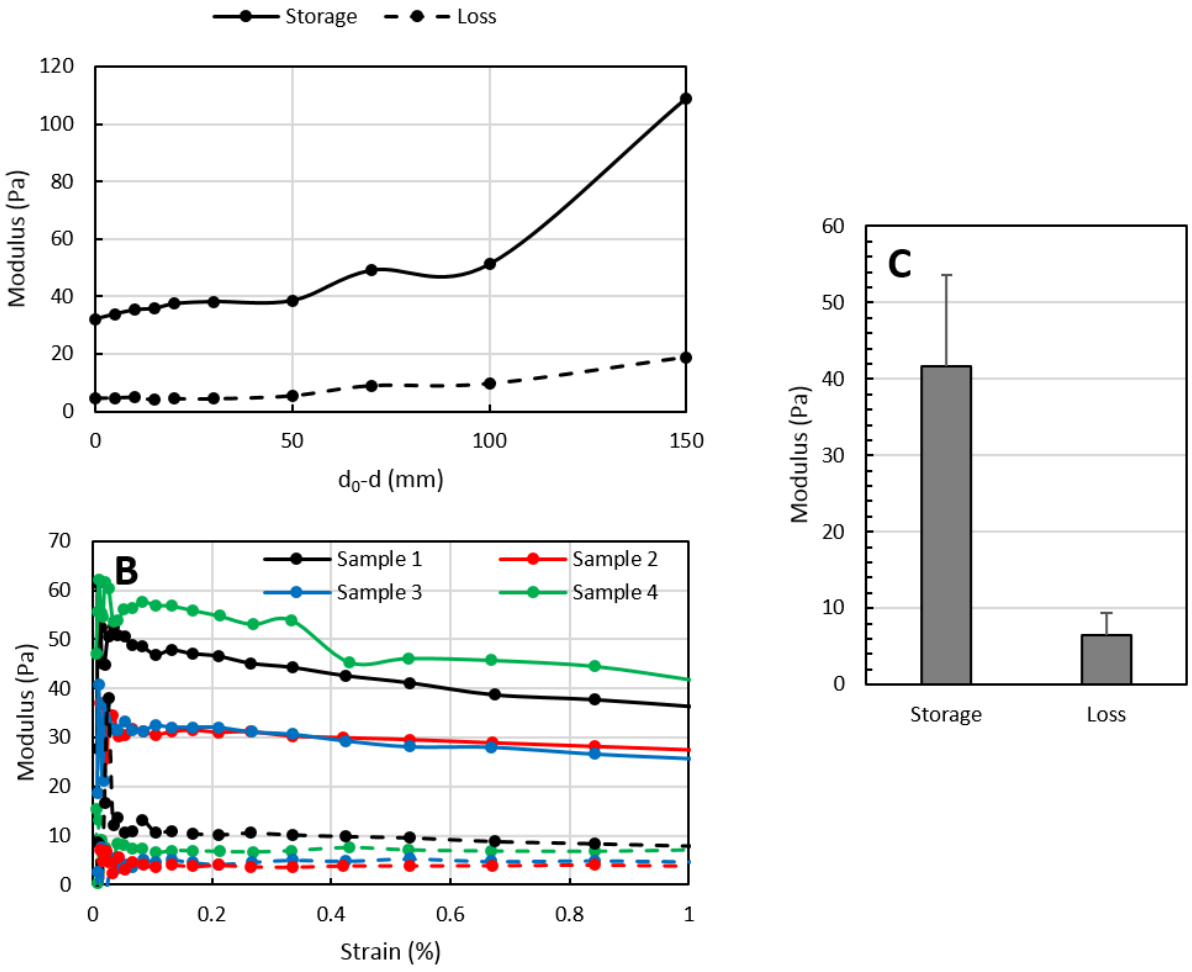

Figure 8. Mechanical characterization of collagen gels. (A) Storage and loss modulus of a collagen gel increase as the rheometer top plate is lowered below initial contact. (B) Collagen gel mechanical properties stabilize for the first few strain increments and then decreases with increasing strain due to slippage. (C) Final storage and loss modulus of the gels (n=4; data reported as mean +/- standard deviation).

Collagen gels are significantly softer compared to the polyacrylamide gels and their stiffness cannot be tuned as easily. With some preliminary mechanical characterization data (data not shown, collaborating labs), we hypothesized that neutrophil extracellular traps (NETs) produced by neutrophils upon activation with phorbol 12-myristate 13-acetate (PMA) can stiffen the collagen gel network and this – in turn – would mechanically activate adherent cells to generated

larger traction forces. In order to gain some insight into the interaction between the NETs and the fibrous collagen network, we analyzed our samples with Raman microspectroscopy (Figure 9).

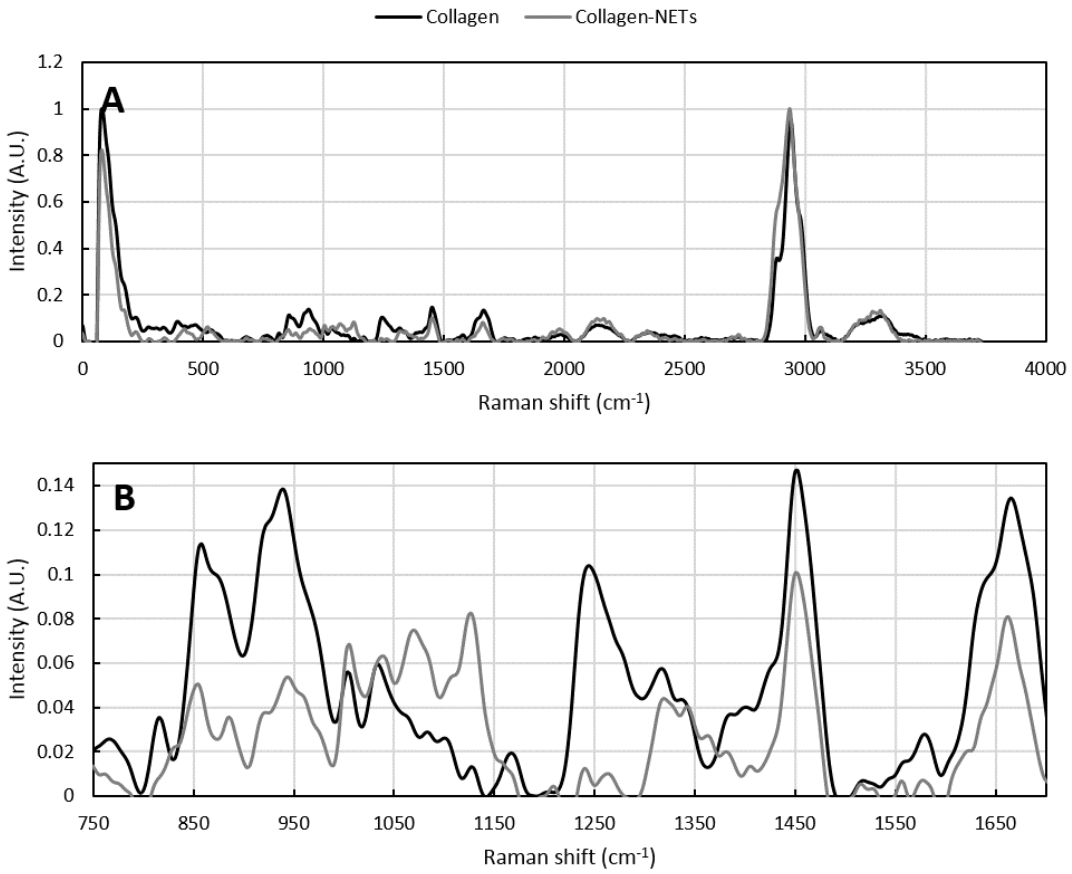

Figure 9. Raman microspectroscopy of collagen gels with and without NETs. (A) Overall Raman spectrum for both gels appears similar, but slight differences are visible in (B) the fingerprint region.

The Raman spectrum obtained for the pure collagen gel contains all the characteristics specific collagen peaks (69,70). The resulting complete Raman spectra appear to be similar for collagen with and without NETs. However, there appears to be some slight differences in the fingerprint region. More specifically, there is loss of the band around 1250 cm^{-1} and gain of two peaks around 1000-1100 cm^{-1} when NETs are introduced into the system. This is most likely attributed to a loss in signal from the collagen through the appearance of other proteins and/or DNA. This leads to the hypothesis that the NETs are physically crosslinking the collagen gel, which causes a loss in signal corresponding to the extended collagen structure at 1250 cm^{-1} and can be indicative of collagen stiffening. The gain in peaks 1000-1100 cm^{-1} could just be the signal from either the residual PMA or new proteins.

3.3.4 Fibroblast traction forces on collagen gels

With some of our collagen gel mechanical characterization data, we ran traction force experiments for fibroblast cultured on collagen with and without NETs (Figure 10A). Compared to the polyacrylamide TFM system, we were presented with some difficulties. First, the collagen gels do not have such a flat top surface, which made it particularly difficult to focus on the uppermost fluorescent bead layer. Second, the gel are much softer and more fragile, which made handling challenging. Third, the SDS killing agent degrades the collagen and precludes an appropriate TFM analysis. We had to resort to using a 0.1% Triton-X solution to carefully lyse the cells without damaging the collagen gel. After overcoming these challenges, we were able to obtain useful measurements.

Qualitatively, it was clear that fibroblasts displaces the beads significantly more on these gels compared to the polyacrylamide substrates (Figure 10B). After obtaining the displacement and stress plots, a much larger region of active bead movement can be identified. The cells appear to pull much more of the collagen surface towards them, creating the observed large displacement field (Figure 10C/E). For both the polyacrylamide and the collagen TFM system, the displacements are about the same in magnitude; however, the stresses required to achieve these displacements are significantly lower for the collagen substrates as expected from a much softer material.

When comparing the two collagen gel conditions, both the displacements and the stresses are surprisingly similar in magnitude. Since the NET-filled collagen gel is expected to be stiffer, one would expect the forces to reflect that. Instead, the main difference between the two conditions is the size of the active displacement field. In the collagen-NETs condition, it seems as though the fibroblasts are unable to pull as much of the collagen when compared to those grown on pure collagen gels. From the traction magnitude plots, it is also apparent that there are many more maximal traction hotspots in the NET-filled collagen condition. Overall, this very preliminary data raises the hypothesis that NETs bind to the individual collagen fibers and locally stiffen the collagen matrix, preventing fibroblasts from extensively deforming it.

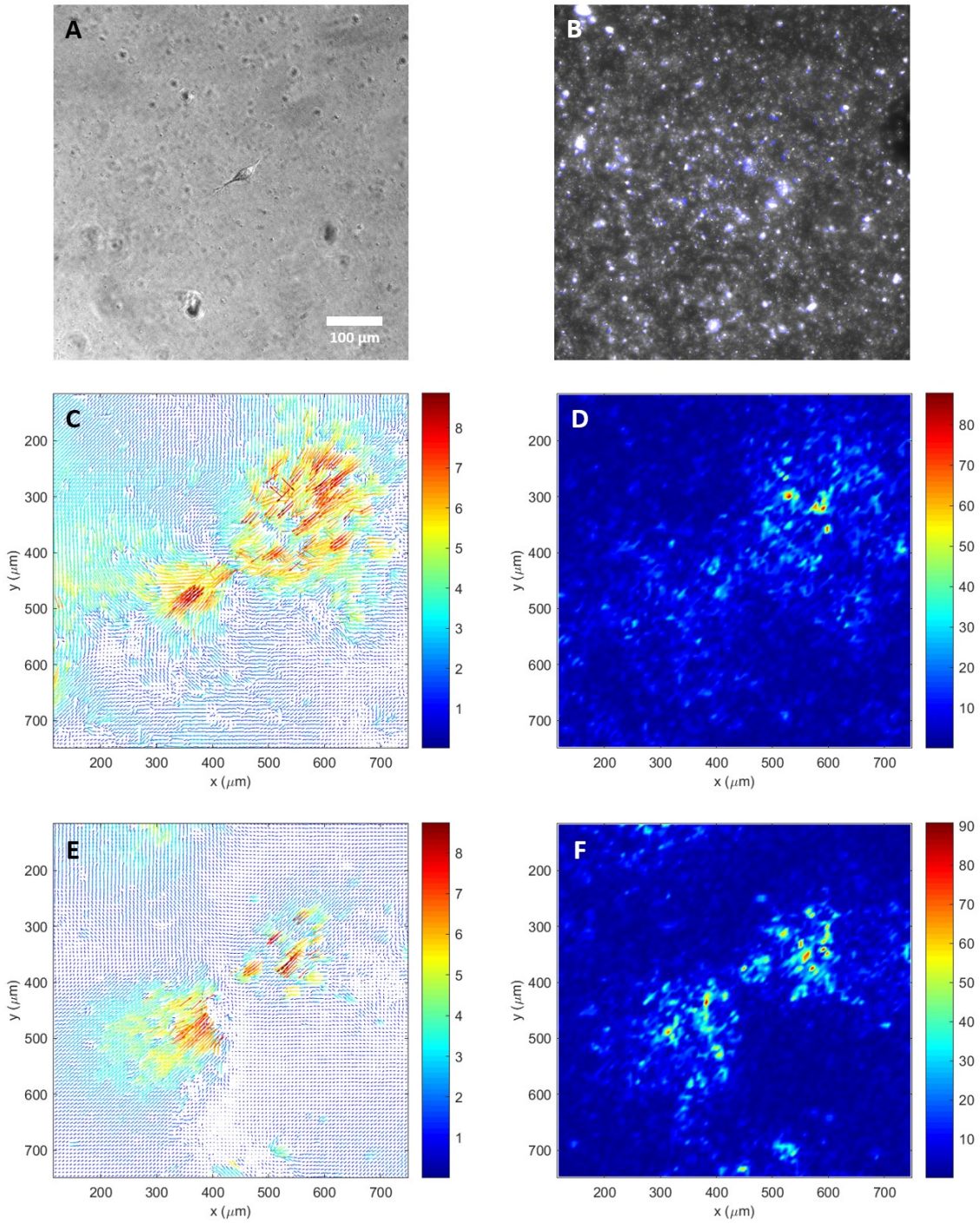

Figure 10. Fibroblast traction forces on collagen gels with and without NETs. (A) Phase contrast image of a fibroblast cell on a soft collagen gel. (B) Fluorescent confocal image stack (grey corresponds to the reference state obtained after cell detachment and blue indicates observed bead displacement). (C/E) PIV vector field (displacements in µm) and (D/F) traction force magnitude (stresses in Pascal units) plots for the collagen (C-D) without and (E-F) with NETs conditions.

3.4 Discussion and impact

Collagen-functionalized polyacrylamide hydrogels present themselves as an ideal controlled platform to quantify traction forces produced by cells that attach and spread on its surface. Without much troubleshooting, the polyacrylamide TFM system can be implemented to measure forces in the 0.5 to 3 $\mu N/\mu m^2$ range produced by single fibroblast cells, consisted with the TFM literature (71,54,72). This system is also robust enough that it can be implemented to measure the stresses produced by grouping of cells as we demonstrated with the BeWo cell colonies here.

Delving deeper into those results raises some interesting questions, considering that BeWo cells are a human trophoblast-derived choriocarcinoma cell line that can be used as an *in vitro* model of the placenta syncytiotrophoblast layer. In fact, BeWo cells can fuse when activated with a fusion-inducing agent such as forskolin for 48 hours, producing an *in vitro* variant of the uppermost cell layer of the placenta (73). Previous data shows that BeWo cells fuse better when they are confined within micropatterns, particularly small ones, as opposed to unconfined controls (Figure 11). Another striking observation is that these cells fuse preferentially in the colony center for the 200 μm micropattern (Figure 11A-B), whereas fusion is more heterogeneous within the larger pattern (Figure 11C) (74). This aligns quite nicely with the stress profiles obtained with the TFM experiments and raises the hypothesis that confinement establishes a traction force pattern within the colony that promotes BeWo cell fusion. Furthermore, the stress ring formed along the colony edge and the smooth traction force levels maintained within the smaller colony could be responsible for promoting more homogenous fusion when compared with the heterogeneous stresses created in the larger colony.

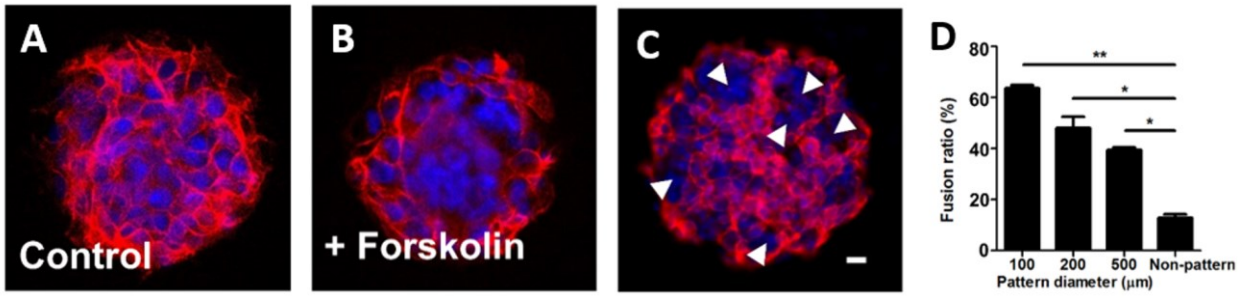

Figure 11. BeWo cell fusion is enhanced in smaller micropatterns. (A) BeWo cells cultured in a 200 μm micropattern without and (B) with fusion inducing agent after 48 hours. (C) Fusion-induced BeWo cells in a larger 500 μm micropattern (white marks represent fused syncytial patches). (D) Fusion ratio is significantly greater in smaller micropatterns (adapted from (74) with permission from ACS publications).

Of course, the traction force microscopy system developed here cannot be directly compared to the micropatterns used for the confined fusion assay. The micropatterns are made on glass using a cell-repellent agarose template, forcing the cells to form colonies within the patterns. Clearly, there is a very large mismatch in terms of substrate stiffness; however, BeWo cell attachment to the fibronectin adhesive patterns on the hydrogel can be considered a reasonable comparison to the actual micropattern setup since TFM cannot be performed on substrates with a stiffness approaching glass. Despite this major limitations, the work presented here has important implications and can help guide future research into placental fusion mechanobiology.

In comparison to polyacrylamide hydrogels, collagen gels are not as easy to implement in the context of traction force microscopy and an attempt to do so encounters many limitations. Even though we were able to rheologically test the mechanical properties of collagen gels reasonably well, there is much more characterization to be done to account for viscoelasticity and plastic behavior. Furthermore, the traction force calculation procedure will have to be extensively modified in order to account for collagen's non-linear mechanical behavior. To properly determine the stresses generated by cells, the displacement of the beads has to be tracked over time. This imposes significant barriers in developing an adequate collagen gel TFM protocol. That being said, the bead displacement values presented here are accurate, but – since no time dynamics are captured during the PIV analysis – the calculated traction forces are most likely inaccurate and cannot be interpreted as absolute. Furthermore, the NET-filled collagen gels have not been tested on the rheometer and their stiffness was assumed to be two times larger than that of the normal collagen gel, according to some preliminary tests. As a result, the data presented here is really only preliminary.

In the context of cancer and the tumor-associated microenvironment, neutrophils are recruited from the bloodstream to enter the affected tissue. There is evidence that the NETs produced by the neutrophils promote cancer cell invasion *in vitro* (75). The work presented here could be a stepping stone in elucidating the mechanism behind this phenomenon. Histology data presented in Figure 12 highlights differences in neutrophil extracellular trap morphology within and outside a lung tumor. NETs appear more elongated and seem to line the honeycomb structure of the lungs. Inside the tumor, however, the NETs are more compact due to the lack of space and the stiffer tissue. Along with the results presented here and these observations, a reasonable

hypothesis could be that NETs are responsible for magnifying the stiffness gradient between the tumor and the surrounding tissue, and thus promoting cancer invasion and ultimately metastasis.

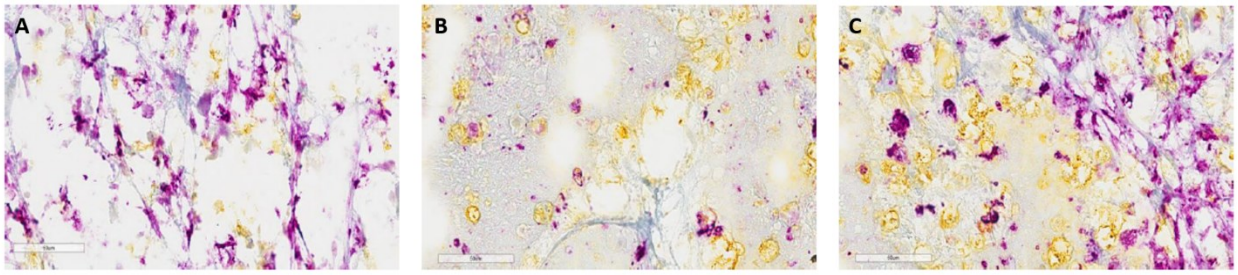

Figure 12. Histology of cancer-affected lung tissue. (A) Relatively normal honeycomb lung structure visible with large NETs (shown in purple) as opposed to (B) dense lung tumor tissue with condensed and compacted NETs. (C) A clear boundary is visible at the interface of the tumor and the normal lung tissue.

3.5 Future directions

To determine whether there are significant differences between the traction force profiles established in the different micropatterns and whether they are correlated with observed BeWo cell fusion patterns, additional experiments are necessary. More specifically, the stress profile data obtained for the BeWo cell clusters is limited to only two cases and thus cannot be tested for significance between the two colony sizes. To further develop the hypothesis that the specific stress patterns produced in the colonies correlate with cell fusion, it would be appropriate to induce fusion and determine whether fusion matches with the low stress regions indicated by the TFM experiment. It would be even better to try to measure traction forces during the fusion process with live imaging and obtain more direct evidence that traction forces play a significant role in initiating fusion.

Similarly, in terms of the collagen gel TFM experiments, the traction forces were analyzed for only two cells, one for each condition, which makes the results quite preliminary and their interpretation speculative at best. Furthermore, due to unforeseen circumstances out of our control, we were unable to mechanically characterize the NET-filled collagen gels, which forced us to assume their stiffness. Properly characterizing the viscoelastic characteristics of both of the collagen gels, running more controlled Raman spectroscopy analyses and performing additional TFM experiments are necessary to continue with this work. Alongside these crucial experiments, the addition of DNAse to the culture medium and actomyosin staining can useful in highlighting the mechanisms driving the observed fibroblast-collagen dynamics.

Chapter 4:
Measuring forces within multicellular spheroids using deformable stress gauges

4.1 Background

Simulating biological systems in order to analyze the forces driving them and quantifying cell traction forces on more realistic collagen matrices proved to be ripe with challenges, stemming mostly from the material complexity of tissues and native biological materials. However, traction forces generated by cells attached to synthetic mechanically-defined substrates such as polyacrylamide could be measured quite reliably. In order to bridge these two worlds and measure cell-generated forces within *in vivo*-like tissues accurately, one could envision designing artificial sensors that can be placed directly into the tissue of interest and whose behavior within this biological system can be analyzed to obtain valuable information about the mechanical forces at play within it.

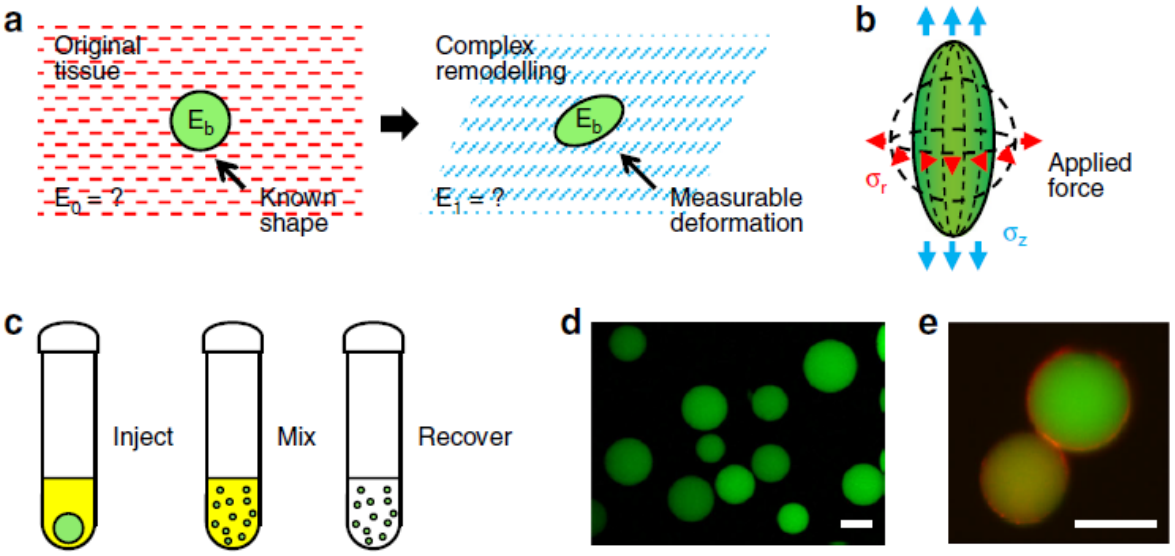

Figure 13. Conceptual overview of the microspherical stress gauge (MSG) system. (a) Soft, compressible and fluorescently labeled hydrogel microspheres can act as sensors of cell-generated mechanical stress, based on changes in sensor shape when embedded within model tissues. (b) Measuring deformation of the hydrogel microspheres is sufficient to calculate the local isotropic and anisotropic stress components in the surrounding remodeling tissue. (c) To fabricate the hydrogel MSGs, aqueous polyacrylamide components and fluorescein methacrylate monomers were mechanically dispersed in an immiscible kerosene phase, and allowed to polymerize, producing (d) fluorescently labeled polydisperse MSGs (green; scale bar =50 μm). (e) Functionalization of the MSG surface with collagen I (red) produces an extracellular matrix coating that is limited to the surface of polyacrylamide microspheres, that facilitates incorporation of the MSGs into engineered tissues (scale bar =25 μm) (taken from (76), following open access reuse terms).

To achieve this goal, we used an inverse emulsion polymerization approach to produce small polyacrylamide hydrogel beads, functionalized them with collagen (Figure 13) and then embedded them in spheroid tissues (76). In a successful attempt to make the beads fluorescent, we also made them unintentionally so soft (~150 Pa in elastic modulus) that they deformed significantly under the action of cells surrounding them. We reasoned that changes in the shape of these microspherical stress gauges (MSGs) could be used to measure cell-generated mechanical forces (Figure 14).

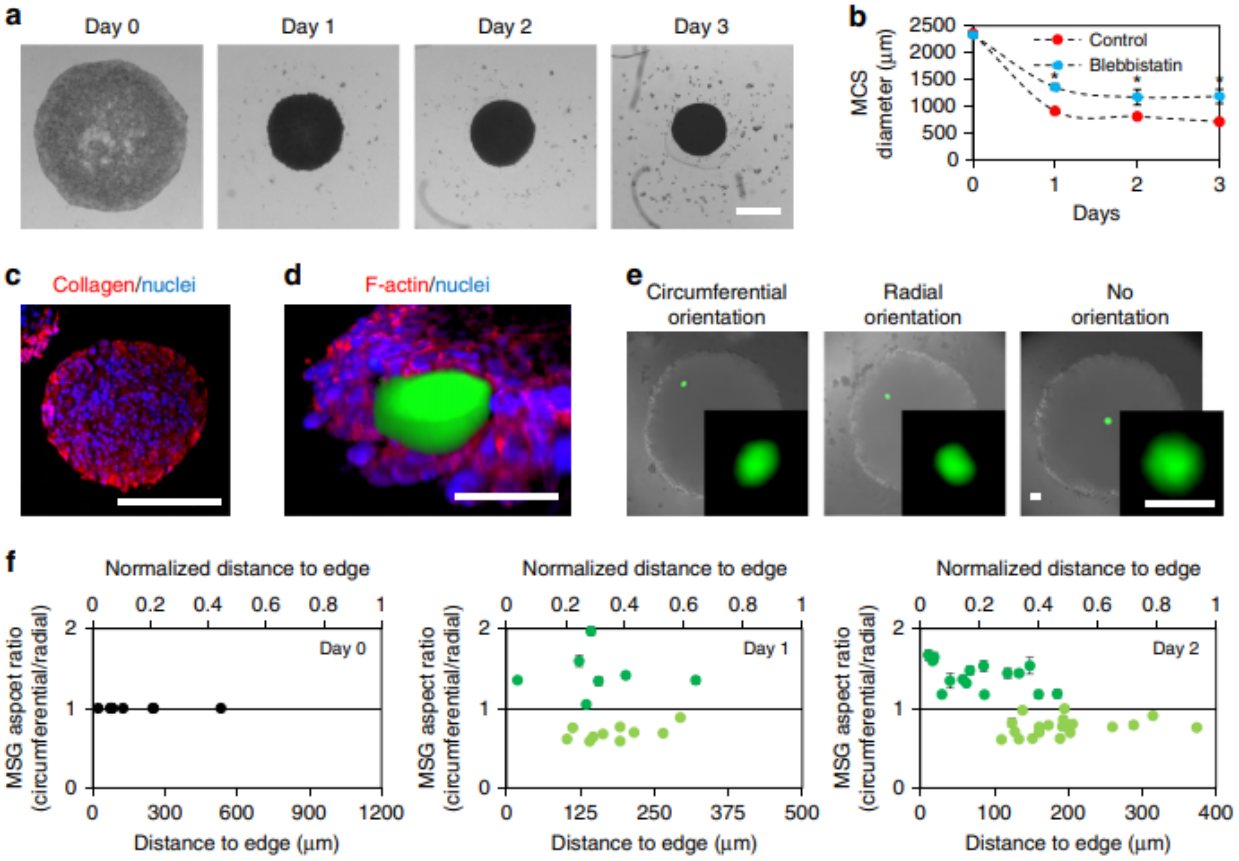

Figure 14. Characterization of multicellular spheroid cultures and MSG incorporation into MCS cultures using standard spheroid-forming techniques. Representative images of spheroid compaction (scale bar = 500 μm). (b) Quantification of spheroid size. Substantial compaction occurs over the first 24 h, and is significantly reduced when actomyosin contractility is inhibited with blebbistatin. Data reported as mean ± standard deviation, n = 9, *p < 0.05 (ANOVA with Tukey post-hoc pairwise comparisons). (c) HS-5 fibroblasts deposit collagen I over 2 days of culture in MCS (scale bar = 250 μm). (d) 3D confocal reconstruction of MSG (green) embedded at the edge of a spheroid at day 2 of culture (scale bar = 50 μm). (e) Embedded fluorescent sensors deform within the spheroid, with circumferential, radial, or no orientation (scale bar = 50 μm), based on position within the spheroid. (f) Quantification of MSG aspect ratio (circumferential MSG dimension/radial MSG dimension) reveals a spatial pattern in the orientation of the MSG deformation, with predominantly circumferential orientation (dark green) at the edge of MCS, and radial orientation (light green) towards the core by day 2 in culture. Data reported as mean +/- standard deviation; n = 9, 17, and 35 for days 0, 1, and 2 (taken from (76), following open access reuse terms).

In order to transform measurable sensor deformations (Figure 14f) into useful stress values, we required a model that could be used to analyze the shape of each sensor to determine what were

the mechanical forces the cells produced to deform it into that specific shape. To this end, in this final section, I develop finite element models to generate sensor calibration plots and use these to create a computational procedure that would allow to quantify forces within multicellular spheroid tissues.

4.2 Methodology

4.2.1 Finite element modelling of MSG deformations

To create standard calibration plots for the deformable hydrogel sensors, 2D axisymmetric finite element models were developed in COMSOL (Burlington, MA, USA) to simulate bead deformations and estimate the stresses necessary to produce these deformations. Neo-Hookean material models were implemented to capture the non-linear stress-strain behavior of the soft sensors. Lamé parameters μ and λ were calculated from experimentally-determined material properties as follows.

$$\mu = \frac{E}{2(1+\nu)} \text{ and } \lambda = \frac{E\nu}{(1+\nu)(1-2\nu)}$$

where E is the Young's modulus of the soft hydrogel sensor and ν corresponds to its Poisson ratio.

Bead compression and expansion along the radial and axial directions was simulated with strain conditions applied to the whole solid domain of the sensor. A free quad mesh was used with a mesh element size corresponding to 2% of the sensor diameter and optimized to ensure that the coefficient of variation was less than 1%. Mesh element quality was also maintained above 0.8 at all times. A dual strain parametric sweep was performed to capture all possible bead deformation combinations. Additional sweeps for the Poisson's ratio were carried out to demonstrate the effect of sensor compressibility along with those for the Young's modulus to assess sensor sensitivity and its accuracy at measuring stress values.

4.2.2 Computational analysis of spheroid tissue-associated sensor deformations

The stress-strain results from the COMSOL parametric sweeps were compiled in MATLAB and surface/contours calibration plots were generated using a piecewise linear interpolation fit.

Then, a MATLAB code was written to process sensor deformation data using this interpolation fit and obtain the unique combination of stresses for each sensor's axial and radial deformation paired values. A Monte Carlo error propagation method was also implemented within the code using a script (77) modified to be compatible with the interpolation fit functions in order to perform a precision error analysis on the sensor stress measurements. Each sensors embedded within the spheroid tissues was subjected to a rigorous image analysis where three perimeter tracings were performed to obtain mean radial and axial strains values along with their corresponding standard deviations. Using these values, the script generated Gaussian probability distribution functions for both axial and radial strains, and used these to generate 10,000 random axial and radial strain values using the MATLAB function `normrnd`. The random strain values were then used to sample the piecewise linear interpolation fit to obtain Monte Carlo statistical distributions for axial and radial stress, which yielded mean stress values and their corresponding 95% confidence intervals.

4.3 Results

4.3.1 Mechanical characterization of the soft deformable sensors

The addition of chain-terminating fluorescent monomers to the polyacrylamide matrix reduces the stiffness of a bulk cylindrical gel about five-fold as determined by shear rheometry (76). However, bulk mechanical characterization of large gels might not be directly applicable to the small 50 μm sensors, which are produced using a different fabrication method. In order to accurately determine the stiffness of these sensors, we built a finite element model that relates bulk rheological findings to results obtained from osmotic pressure tests (Figure 15) since their small size and softness make it quite challenging to use conventional atomic force microscopy techniques for characterization. The sensors were placed into a 100 mg/mL long-chain dextran solutions, which causes them to shrink due to the applied osmotic pressure (Figure 15a). The dextran polymer chains are too large to enter the pores of the polyacrylamide hydrogel beads and the resulting pressure differential forces water out of the microspheres, which then causes the beads to shrink with respect to their mechanical properties (Figure 15b-c). To estimate the osmotic pressure created by this solution, a 2D axisymmetric model was built in COMSOL (Burlington, MA, USA) to simulate isotropic pressure-induced deformation of soft cylindrical gels with mechanical properties determined by rheology. By performing a parametric sweep for external

pressure and using experimental sensor deformation measurements (~0.15 in compressive strain), we determined that a 100 mg/mL dextran solutions exerts an apparent mechanical pressure of 67 Pa on the beads (dashed line in Figure 15d). Using this equivalent pressure as a boundary condition in the sensor deformation model allowed us to perform a sensor material sweep (Figure 15e) and accurately determine their shear modulus at 60 Pa, which corresponds to 156 Pa in stiffness (Figure 15f-g). The Poisson's ratio was separately estimated to be 0.3 (76).

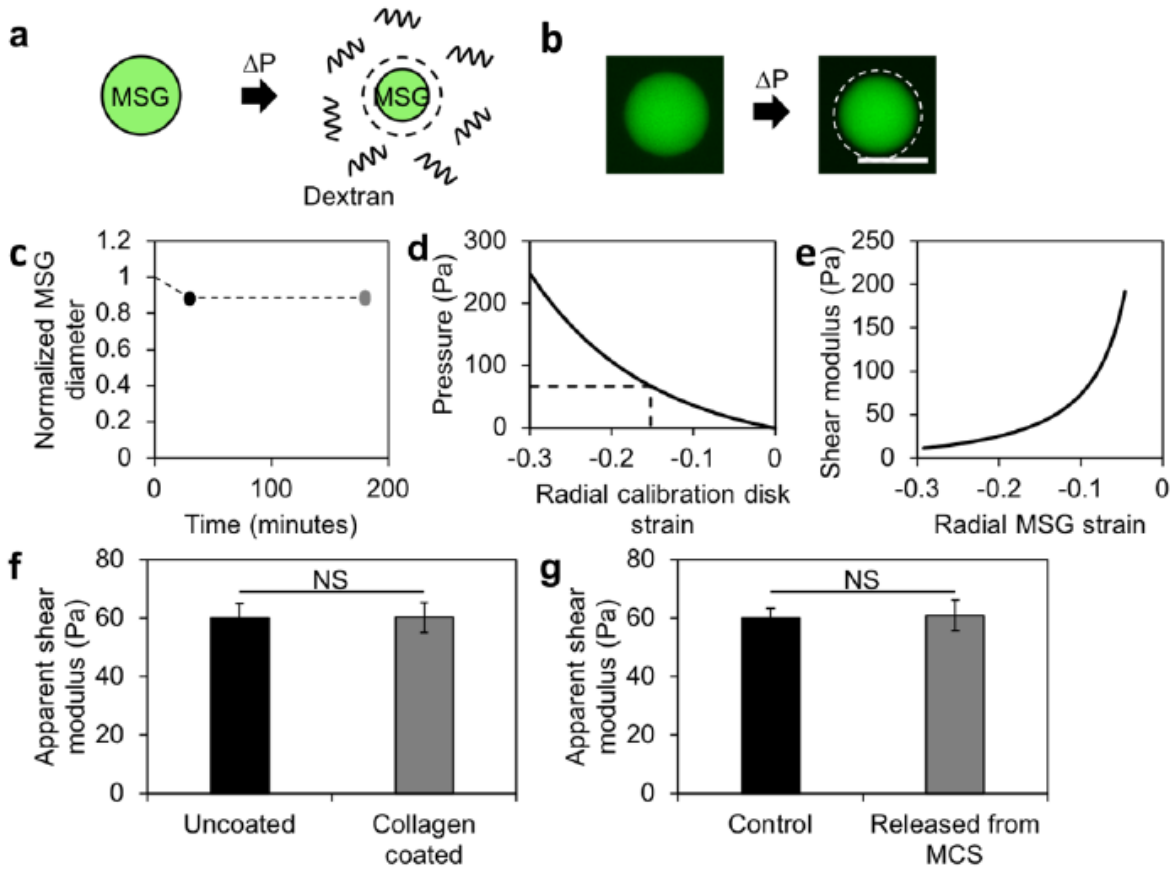

Figure 15. Measurement of MSG mechanical properties by application of osmotic pressure. A schematic representation and (b) fluorescent microscope images (scale bar = 50 μm) depicting hydrogel contraction when exposed to 100 mg/mL of dextran solution. (c) MSG sizes remain constant after 3 hours in the dextran solution, confirming that dextran chains are excluded from the polymer matrix. The system was calibrated against osmotic pressure-induced deformation of a bulk disk-shaped polyacrylamide hydrogel sample (diameter = 13 mm) for which the shear modulus was established using conventional shear rheometry. (d) A finite element simulation was developed to determine the effective osmotic pressure generated by a 100 mg/mL solution of dextran. Next, this osmotic pressure value was applied to (e) a parametric sweep of shear modulus in the isotropic compression of a spherical MSG. (f) Osmotic pressure measurements on MSGs indicates that collagen coating does not significantly alter mechanical rigidity of the MSG (n = 24, p = 0.782). (g) No significant differences were found between coated MSGs (control) and MSGs that had been removed from spheroids after two days of culture by detergent-based extraction (released), demonstrating that MSG properties remain constant even after embedding within the tissue of interest (n = 16-19, p = 0.837). All data reported as mean +/- standard deviation. NS indicates no significant differences (one-way ANOVA with Tukey post-hoc pairwise comparisons) (taken from (76), following open access reuse terms).

4.3.2 Finite element modelling of sensor deformations

After accurately determining the stiffness and the Poisson's ratio of these sensors, we built a 2D finite element model (Figure 16) that simulates sensor deformations in axial and radial directions. Utilizing the inherent symmetry in our system, the model was simplified by considering a rotating half-sensor geometry (Figure 16a). Radial and axial deformation strains were applied onto the bead domain, instead of its boundaries, in order to ensure uniform strains and a proper displacement field within the sensor (Figure 16b). The model produced uniform radial and axial stresses from simulated bead deformation conditions and these values could be directly read from the simulations (Figure 16c-d).

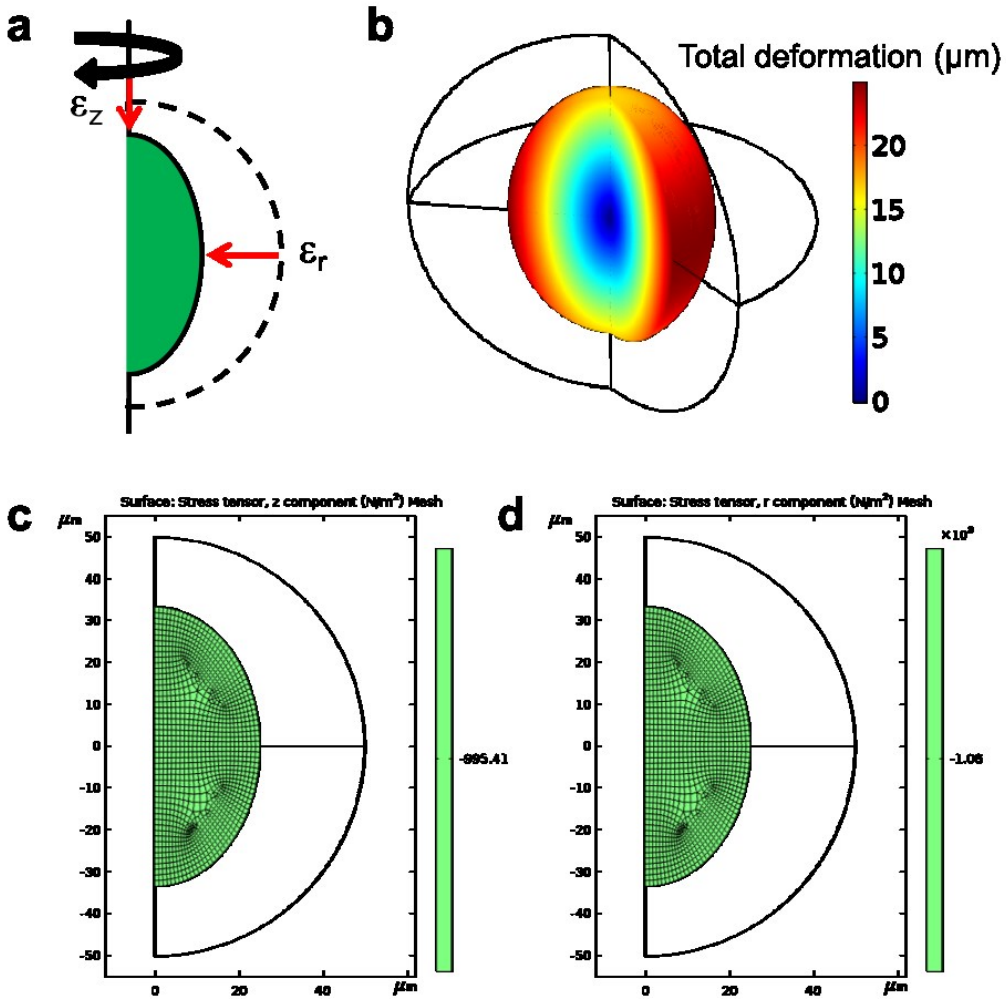

Figure 16. Finite element model to simulate multiaxial MSG deformation.. (a) Schematic of the 2D axisymmetric model along with strain conditions applied throughout the bead domain. (b) Representative image of a partially revolved axisymmetric MSG bead deforming under -0.33 axial strain and -0.5 radial strain domain conditions. Corresponding (c) axial and (d) radial stresses are confirmed to be uniform throughout the sensor (taken from (76), following open access reuse terms).

I also ran a parametric sweep for the Poisson's ratio (Figure 17) to see whether compressibility is an important design consideration in this system. In the perfectly compressible case, the calibration plot appears flat and the soft hydrogel sensors do not required much stress to deform (Figure 17a). As a result, the sensor essentially becomes insensitive to the stresses applied to it. However, it is still possible to distinguish between the two stress directions. In the extreme polar opposite case, incompressibility makes it impossible to resolve any kind of stresses (Figure 17c). Clearly, a reasonably compressible sensor is necessary to measure significant isotropic and anisotropic stresses, which is the case for these stress gauges (Figure 17b).

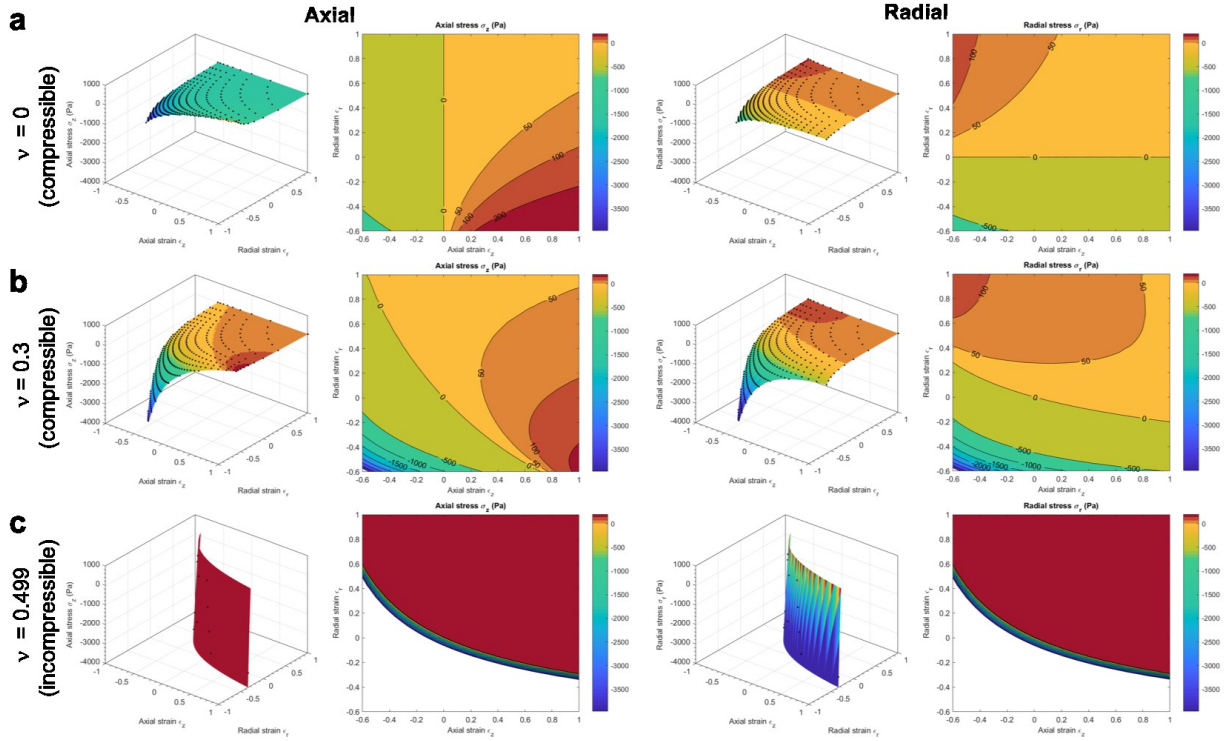

Figure 17. MSG calibration plots obtained following a Poisson's ratio parameteric sweep.. Finite element simulations relating axial (z) and radial (r) stresses with axial and radial strains for (a) perfectly compressible (ν = 0), (b) actual (ν = 0.3) and (c) incompressible (ν = 0.499) materials. For perfectly compressible materials, strains in the axial and radial directions are only weakly coupled to radial and axial stresses respectively. On the other end of the spectrum, as the material approaches (c) incompressibility (ν = 0.499), microsphere deformations cannot be resolved into unique combinations of axial and radial stress. Hence, the use of compressible materials enables the measurement of both isotropic and anisotropic stress components in the system (taken from (76), following open access reuse terms).

4.3.3 Soft hydrogel sensor stress measurements within spheroid tissues

The calibration plots relevant to our sensors (Figure 17b) were then used to process sensor deformation data, obtained from geometric measurements during image analysis, for stress gauges randomly embedded within spheroid tissues and the results are presented below in Figure 18.

Clearly, the MSG system is able to estimate stresses within spheroids that range from 50 Pa in tension up to 1.5 kPa in compression, constituting a large dynamic stiffness measurement range. More interestingly, however, a clear mechanical stress pattern emerges when the stress data is plotted against sensor position within the spheroid. Mechanical stresses appear to be high in compression almost halfway into the tissues at about 150 μm away from the edge. This high compression region within the bulk of the multicellular spheroid is contrasted with much smaller compressive stresses near the spheroid edge. In fact, positive stress values are observed in the circumferential direction at the edge, whereas the radial stresses never go above zero (Figure 18). This suggests that a thin layer of cells at the edge is kept under tension and balances the large compressive forces located within the spheroid. Due to the random sampling nature of the MSG incorporation within the spheroids, conclusion about the forces present within the core of the spheroid cannot be drawn.

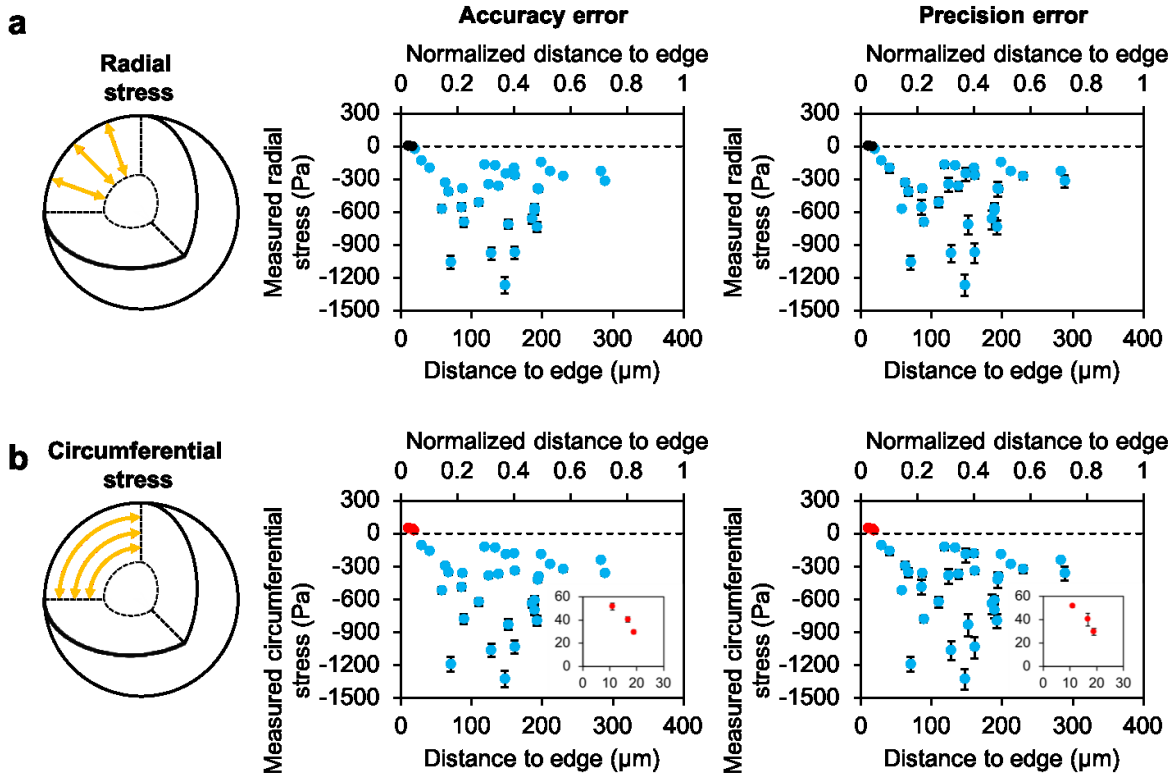

Figure 18. Spatial mapping of cell-generated stresses within 3D fibroblast spheroid cultures.. Comparison of MSG errors associated with uncertainties in MSG modulus (accuracy) and strain measurement error (precision) in the (a) radial and (b) circumferential directions at day 2 of culture. Red data points represent tensional stress measurements, blue data points represent compressional stress measurements, and black data points represent stress measurements close to zero (-10 Pa to +10 Pa). Insets depict closer view of measured tensional stresses. Accuracy errors correspond to errors of 6% in stress readings, while precision errors were generated based on Monte Carlo simulations of error assuming a Gaussian normal distribution of values for repeated measurements of radial and circumferential bead dimensions (taken from (76), following open access reuse terms).

4.3.4 Error analysis on MSG measurements

Since the sensors appeared to be highly sensitive and allowed us to measure a large dynamic range of stresses, we wanted to determine the uncertainty on our stress measurements. To estimate the precision of this sensor system, for each embedded sensor, three sensor perimeter tracings were performed during image analysis to obtain mean radial and axial strains along with their associated standard deviations. A Monte Carlo uncertainty propagation was then performed using these values. By generating Gaussian probability distribution functions for both strains and probing the non-linear interpolation stress fits using strains randomly generated from the distribution functions, the uncertainty on the stress values in the form of 95% confidence intervals could be determined (Figure 19) and was included for each point in Figure 18 as precision error.

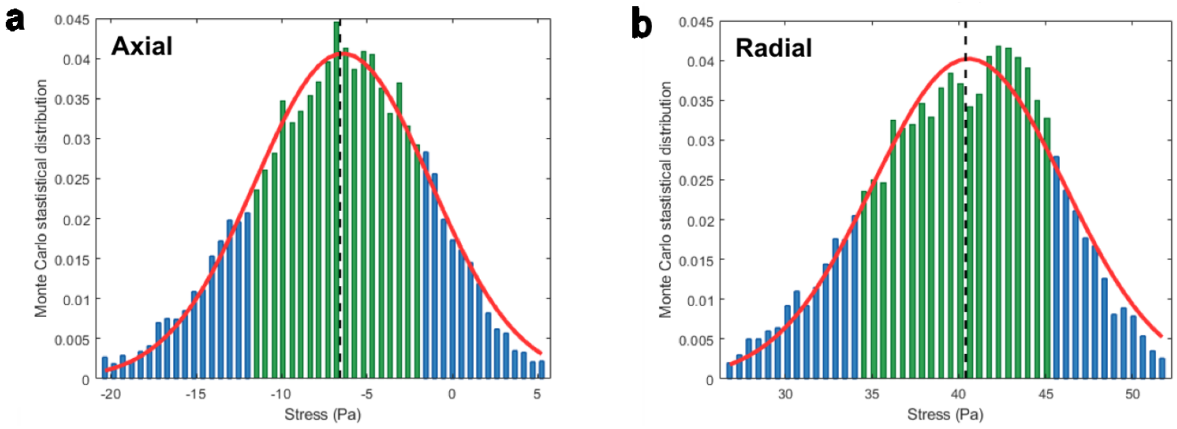

Figure 19. Representative bar graphs of Monte Carlo estimates in stress measurement uncertainties arising from errors in measurement of MSG deformation.. Repeated measurement of MSG dimensions was used to estimate the precision error in analysis of MSG size along the axial and radial axes. Assuming a Gaussian normal distribution of measurements in both the radial and circumferential axes for each data point, 10,000 randomly generated deformation values were converted to stresses through the non-linear interpolation function. (a, b) Representative datasets from (a) axial and (b) radial stress Monte Carlo statistical distributions for a single axial compression-radial tension MSG data point (-6.5 Pa in the axial direction; +40.5 Pa in the radial direction). Mean stress values (dashed line) and their respective 95% confidence intervals (green section) are obtained empirically from the randomly generated dataset around each point. Similar curves were generated for every data point analyzed, and the 95% confidence intervals for each point are plotted as estimates of precision error in Figure 18 (taken from (76), following open access reuse terms).

Aside from measuring the extent of sensor deformation during image analysis, an additional source of error could be the mechanical characterization of the microspherical hydrogels. In fact, the uncertainty on the stiffness was about 3.45 Pa in shear modulus or 10 Pa in Young's modulus. To determine the accuracy of the MSG system, a parametric sweep for Young's modulus was implemented in the sensor deformation finite element model. Deviations of 10 Pa in sensor stiffness lead to an error of 5.77% on each stress measurement and this error was included as

accuracy error in Figure 18. Considering both types of errors in this system, tensional stress values of 50 Pa only had a maximal error of about 8 Pa, whereas larger 1.5 kPa compressive stresses had an uncertainty of approximately 120 Pa. Taken together, this only constitutes a measurement error of about +/- 16% on each stress value.

4.4 Discussion

The mechanical characterization of the microspherical stress gauges presented here was very extensive, but – due to their minuscule size – did not consider whether the material is homogenous and the material properties were assumed to be uniform in the deformation analysis. Oxygen is known to inhibit the polymerization of polyacrylamide and could lead to material inhomogeneity. However, since the sensors are produced in a degassed oil phase and the precursor solution was well mixed before gelation, it is highly unlikely that the sensors exhibit material anisotropy and the material homogeneity assumption is valid. The decision to have a uniform strain field within the hydrogel domain is then also justified.

On the other hand, the assumption that the soft hydrogel sensors are of ellipsoidal geometry and have at least one axis of symmetry as implemented in the analysis presented here is valid for the case of the symmetric multicellular spheroid tissues and significantly facilitates the deformation analysis. However, this simplification might not be applicable to non-symmetrical tissues and presents itself as a limitation. This can be addressed by implementing a 3D sensor deformation analysis. For example, Mohagheghian et al. were successfully able to spatially map the deformation of their elastic round microgel sensors in 3D and then to translate these measurements into stresses (78). However, finite element approaches are resource-intensive, particularly when simulating 3D deformation fields. Fortunately, methods that do not rely on finite elements have recently been implemented to this end (79,80). Vorselen et al. addressed the problem through optimization by iteratively guessing surface displacements and tractions until a cost function was minimized and, with this approach, determined the forces at play during phagocytosis. Perhaps slightly faster than a full finite element simulation, this method is still quite computationally intensive (79). On the other hand, Kaytanlı et al. developed a rather computationally simple and rapid procedure that determines 3D cell traction forces exerted on compressible hydrogel microsensors from confocal slice images of their sensors using an analytical procedure (80). To obtain the complete 3D displacement field that characterizes the

shape change of their sensors, they first assumed a homogenous sensor deformation into an ellipsoid and then considered the small radial displacements that give rise to the final sensor shape. Implementing one of these approaches in our system would make our system much more broadly applicable to any non-symmetrical tissue.

Another decision made in the analysis presented here is that cells apply normal non-dissipative forces onto the sensors and shearing can be neglected. If cells were to apply significant shear stresses onto the MSGs, they would rotate or move significantly within the multicellular spheroids. However, these are tightly packed and produce only a limited amount of extracellular matrix. Furthermore, the MSGs are small compared to the overall tissue and are coated with collagen, which helps them incorporate within the spheroids and prevents them from acting as a void in the tissue. As a result, this decision is justified in the case of spheroids, but has profound implications if this technology is to be used in other less cell-packed ECM-rich tissues. In those application, the deformation analysis would have to better model the tissue-sensor interface of that specific tissue to account for slip and/or stiffness mismatch. In any case, another concern is the effect of MSGs on tissue dynamics. The inclusions of these sensors could adversely affect the development and formation of spheroids, as the tissues could perhaps see it as foreign and try to extrude it out into the media.

4.5 Impact

Biological tissues and natural biomaterials have highly non-linear mechanical properties that vary with time and depend on cellular activity, which makes their material characterization a daunting task and precludes any accurate analysis of the mechanical behavior of the cells that make up these tissues or are grown on these *in vivo*-like matrices. Using soft deformable mechanically-defined hydrogel sensors and a robust finite element sensor model, we were able to quite accurately and precisely measure the cell-generated mechanical forces present within 3D multicellular spheroid tissues without requiring any detailed material understanding of this biological system. The microspherical stress gauges are functionalized with collagen and are small enough that they integrated well into the multicellular spheroids and made it possible to spatially map the mechanical stresses within the spheroids without disturbing them. The results presented here suggest that a thin tensional skin holds a highly compressive bulk spheroid in mechanical balance. With some additional staining experiments, we confirmed that this stress pattern matches known

mechanobiological markers such as F-actin, phosphorylated myosin and YAP/TAZ nuclear localization (76), and that the edge cells are in fact more mechanically active, contracting to produce the observed tensional skin.

Multicellular spheroids are widely used as an *in vitro* model tissue for drug screening and tissue engineering, and are often implemented as surrogates for tumors in cancer research (81–83). Mathematical modelling (84,85) and observations that tumors release stress and change shape when dissected (86) have supported the underlying premise that a tensional layer balances the internal tumor solid stress, which is generated by tumor growth. However, after our spheroid proliferation tests came back negative, this work along with additional computational experiments indicate that the stress patterns measured in the multicellular spheroids are due to the active thin tensional skin and the outside-in contraction it generates creates the highly compressive stresses observed within the spheroid rather than proliferation in the core (76). The hypothesis developed here is that high nutrient and oxygen availability at the surface of the spheroids promotes cells to be more mechanically active and generate outside-in contraction, whereas cells inside of it are less active due to a limited nutrient and oxygen supply. It is still unclear whether these conclusions are applicable to *in vivo* tumors, which essentially grow starting from a single cell and are not produced by cell aggregation as is the case here. However, this work does indicate that tissue formation, whether it occurs spontaneously in the body or is engineered in the lab, itself plays a key role in determining the ultimate mechanical state of the tissue.

The microspherical stress gauge system presented and developed here provides a unique opportunity to visualize the forces present in biological systems and to study the interplay between mechanical forces and biological function. Not only can this system be used to monitor the mechanical status of a tissue, it can also be used to learn how cells self-organize into functional tissues and how they interact with their environment. This knowledge can even be harnessed to develop new tissue engineering strategies that leverage nature's self-organizing capabilities in order to achieve ultimate control over tissue structure and function *in vitro*.

Chapter 5: Conclusion

From the perspective of physics, cells cannot be simply treated as inert materials since they can spontaneously decide to move, eat their environment and then rebuild it to their liking. For a long time, they have been treated as black boxes subject to natural principles, but – now that the tools necessary to study them have been created – we can start to understand their inner workings. To further complicate the matter, cells can join forces and become one powerful unit that has a mind of its own.

In this thesis, I attempt to quantify the mechanical forces generated by cells and tissues using various engineering tools in three different circumstances. More specifically, in the first section, I developed finite element simulations of the wound retraction process in a pre-stressed collagen model tissue that is actively punctured with a needle. In order to properly simulate this process, we had to define the mechanical properties of the microtissue, which turned out to be a challenge on its. We implemented an inverse finite element procedure and utilized existing literature collagen tissue material data to determine the most appropriate material definition for our microtissue system. Although not perfect, a viscoelastic formulation combined with time-dependent plasticity was enough to describe wound retraction and run the necessary simulations to observe that a significant long-lasting hoop stress is created near the wound edge. Along with additional experiments, these simulations gave light to the hypothesis that tissue retraction after wounding mechanically promotes future wound closure via the hoop stress established during injury.

In the second section, I utilized synthetic polyacrylamide gels as well as natural collagen hydrogels to create traction force microscopy substrates and then used them to measure the stresses generated by cells as they pull on them. We were easily able to measure the traction forces of single fibroblast cells as well as those of BeWo cell colonies on the synthetic substrates. Most notably, we observed that smaller colonies of cells produce more homogenous inward stresses that peak at the colony edge and we speculate that this specific force pattern can promote BeWo cell fusion into a syncytium. Implementing the same traction force microscopy protocol for the collagen substrates proved to be much more difficult and many questions are yet to be addressed. Nevertheless, our collagen gel traction force experiments bring forward an interesting idea that neutrophil extracellular traps produced by leukocytes bind to collagen fibers, locally stiffen the

matrix and drive an increase in fibroblast traction forces, and could have potential implications in cancer research.

In the final section, we developed microspherical stress gauges (MSGs) that we embedded into multicellular spheroid tissues in order to spatially map the stresses that are maintained within them. I ran finite element simulations and developed a computational procedure to analyze the deformations of these soft hydrogel sensors and translate them into useful stress values. As it turns out, highly compressive stresses established within spheroids are kept in check by small tensional stresses at their surface. Contrary to the premise that solid stress within spheroids is created by cell proliferation, we demonstrated with additional experiments that this solid stress is sometimes produced by an outside-in contraction of the small, but active, tensile cell layer at the spheroid surface. We believe that this technology will find many applications in the future and will be instrumental in gaining insight into tissue morphogenesis.

By building compliant hydrogel playgrounds for cells and using powerful computational tools to analyze their behavior as described in this thesis, I hope that I have convinced you that developing engineering tools to probe and analyze cell mechanical behavior can help us better understand, not only what cells are made of, but what they can do.

References

1. Ingber D. Mechanobiology and diseases of mechanotransduction. Ann Med. 2003 Jan 1;35(8):564–77.

2. Tee S-Y, Bausch A, Janmey PA. The mechanical cell. Curr Biol CB. 2009 Sep 15;19(17):R745–8.

3. Holeček M, Kochová P, Tonar Z. Mechanical Properties of Living Cells and Tissues Related to Thermodynamics, Experiments and Quantitative Morphology – A Review. Theor Biomech [Internet]. 2011 Nov 25 [cited 2020 Apr 5]; Available from: https://www.intechopen.com/books/theoretical-biomechanics/mechanical-properties-of-living-cells-and-tissues-related-to-thermodynamics-experiments-and-quantita

4. Mammoto T, Mammoto A, Ingber DE. Mechanobiology and Developmental Control. Annu Rev Cell Dev Biol. 2013;29(1):27–61.

5. Ingber DE, Wang N, Stamenović D. Tensegrity, cellular biophysics, and the mechanics of living systems. Rep Prog Phys Phys Soc G B. 2014 Apr;77(4):046603.

6. Hopyan S, Sharpe J, Yang Y. Budding behaviors: Growth of the limb as a model of morphogenesis. Dev Dyn. 2011;240(5):1054–62.

7. Keller R. Physical Biology Returns to Morphogenesis. Science. 2012 Oct 12;338(6104):201–3.

8. Heisenberg C-P, Bellaïche Y. Forces in Tissue Morphogenesis and Patterning. Cell. 2013 May 23;153(5):948–62.

9. Kim D-H, Wong PK, Park J, Levchenko A, Sun Y. Microengineered Platforms for Cell Mechanobiology. Annu Rev Biomed Eng. 2009;11(1):203–33.

10. Loh O, Vaziri A, Espinosa HD. The potential of MEMS for advancing experiments and modeling in cell mechanics. Exp Mech. 2009 Jan 1;49(1):105–24.

11. Zheng XR, Zhang X. Microsystems for cellular force measurement: a review. J Micromechanics Microengineering. 2011 Apr;21(5):054003.

12. Gauvin R, Parenteau-Bareil R, Dokmeci MR, Merryman WD, Khademhosseini A. Hydrogels and microtechnologies for engineering the cellular microenvironment. WIREs Nanomedicine Nanobiotechnology. 2012;4(3):235–46.

13. Roca-Cusachs P, Conte V, Trepat X. Quantifying forces in cell biology. Nat Cell Biol. 2017 Jul;19(7):742–51.

14. David Merryman W, Engler AJ. Innovations in Cell Mechanobiology. J Biomech. 2010 Jan 5;43(1):1.

15. Fletcher DA, Mullins RD. Cell mechanics and the cytoskeleton. Nature. 2010 Jan;463(7280):485–92.

16. Treiser MD, Yang EH, Gordonov S, Cohen DM, Androulakis IP, Kohn J, et al. Cytoskeleton-based forecasting of stem cell lineage fates. Proc Natl Acad Sci. 2010 Jan 12;107(2):610–5.

17. Di Carlo D. A Mechanical Biomarker of Cell State in Medicine. J Lab Autom. 2012 Feb 1;17(1):32–42.

18. Wang JH-C, Thampatty BP. An introductory review of cell mechanobiology. Biomech Model Mechanobiol. 2006 Mar;5(1):1–16.

19. Jaalouk DE, Lammerding J. Mechanotransduction gone awry. Nat Rev Mol Cell Biol. 2009 Jan;10(1):63–73.

20. Shao Y, Fu J. Integrated Micro/Nanoengineered Functional Biomaterials for Cell Mechanics and Mechanobiology: A Materials Perspective. Adv Mater. 2014;26(10):1494–533.

21. Lacroix D, Planell JA, Prendergast PJ. Computer-aided design and finite-element modelling of biomaterial scaffolds for bone tissue engineering. Philos Trans R Soc Math Phys Eng Sci. 2009 May 28;367(1895):1993–2009.

22. Walpole J, Papin JA, Peirce SM. Multiscale Computational Models of Complex Biological Systems. Annu Rev Biomed Eng. 2013;15(1):137–54.

23. Freutel M, Schmidt H, Dürselen L, Ignatius A, Galbusera F. Finite element modeling of soft tissues: Material models, tissue interaction and challenges. Clin Biomech. 2014 Apr 1;29(4):363–72.

24. Brodland GW. How computational models can help unlock biological systems. Semin Cell Dev Biol. 2015 Dec 1;47–48:62–73.

25. Gurtner GC, Werner S, Barrandon Y, Longaker MT. Wound repair and regeneration. Nature. 2008 May;453(7193):314–21.

26. Dubois SJ, Kalashnikov N, Moraes C. Robust and Precise Wounding and Analysis of Engineered Contractile Tissues. Tissue Eng Part C Methods. 2019 Aug 14;25(11):677–86.

27. Babaei B, Velasquez-Mao AJ, Pryse KM, McConnaughey WB, Elson EL, Genin GM. Energy dissipation in quasi-linear viscoelastic tissues, cells, and extracellular matrix. J Mech Behav Biomed Mater. 2018 Aug 1;84:198–207.

28. Malandrino A, Trepat X, Kamm RD, Mak M. Dynamic filopodial forces induce accumulation, damage, and plastic remodeling of 3D extracellular matrices. PLOS Comput Biol. 2019 Apr 8;15(4):e1006684.

29. Feng Z, Seya D, Kitajima T, Kosawada T, Nakamura T, Umezu M. Viscoelastic characteristics of contracted collagen gels populated with rat fibroblasts or cardiomyocytes. J Artif Organs. 2010 Sep 1;13(3):139–44.

30. Wang H, Svoronos AA, Boudou T, Sakar MS, Schell JY, Morgan JR, et al. Necking and failure of constrained 3D microtissues induced by cellular tension. Proc Natl Acad Sci. 2013 Dec 24;110(52):20923–8.

31. Liu AS, Wang H, Copeland CR, Chen CS, Shenoy VB, Reich DH. Matrix viscoplasticity and its shielding by active mechanics in microtissue models: experiments and mathematical modeling. Sci Rep. 2016 Sep 27;6:33919.

32. Raub CB, Suresh V, Krasieva T, Lyubovitsky J, Mih JD, Putnam AJ, et al. Noninvasive Assessment of Collagen Gel Microstructure and Mechanics Using Multiphoton Microscopy. Biophys J. 2007 Mar 15;92(6):2212–22.

33. Nam S, Lee J, Brownfield DG, Chaudhuri O. Viscoplasticity Enables Mechanical Remodeling of Matrix by Cells. Biophys J. 2016 Nov 15;111(10):2296–308.

34. Ban E, Franklin JM, Nam S, Smith LR, Wang H, Wells RG, et al. Mechanisms of Plastic Deformation in Collagen Networks Induced by Cellular Forces. Biophys J. 2018 Jan 23;114(2):450–61.

35. Wisdom KM, Adebowale K, Chang J, Lee JY, Nam S, Desai R, et al. Matrix mechanical plasticity regulates cancer cell migration through confining microenvironments. Nat Commun. 2018 Oct 8;9(1):4144.

36. Flynn C. Finite element models of wound closure. J Tissue Viability. 2010 Nov 1;19(4):137–49.

37. Cardinal M, Eisenbud DE, Armstrong DG. Wound shape geometry measurements correlate to eventual wound healing. Wound Repair Regen. 2009;17(2):173–8.

38. Sniadecki NJ, Anguelouch A, Yang MT, Lamb CM, Liu Z, Kirschner SB, et al. Magnetic microposts as an approach to apply forces to living cells. Proc Natl Acad Sci. 2007 Sep 11;104(37):14553–8.

39. Bement WM, Mandato CA, Kirsch MN. Wound-induced assembly and closure of an actomyosin purse string in Xenopus oocytes. Curr Biol. 1999 Jun 3;9(11):579–87.

40. Khademhosseini A, Langer R. Microengineered hydrogels for tissue engineering. Biomaterials. 2007 Dec 1;28(34):5087–92.

41. Ullah F, Othman MBH, Javed F, Ahmad Z, Akil HMd. Classification, processing and application of hydrogels: A review. Mater Sci Eng C. 2015 Dec 1;57:414–33.

42. Tse JR, Engler AJ. Preparation of Hydrogel Substrates with Tunable Mechanical Properties. Curr Protoc Cell Biol. 2010;47(1):10.16.1-10.16.16.

43. Antoine EE, Vlachos PP, Rylander MN. Review of Collagen I Hydrogels for Bioengineered Tissue Microenvironments: Characterization of Mechanics, Structure, and Transport. Tissue Eng Part B Rev. 2014 Jun 12;20(6):683–96.

44. Style RW, Boltyanskiy R, German GK, Hyland C, MacMinn CW, Mertz AF, et al. Traction force microscopy in physics and biology. Soft Matter. 2014 May 21;10(23):4047–55.

45. Schwarz US, Soiné JRD. Traction force microscopy on soft elastic substrates: A guide to recent computational advances. Biochim Biophys Acta BBA - Mol Cell Res. 2015 Nov 1;1853(11, Part B):3095–104.

46. Nerger BA, Siedlik MJ, Nelson CM. Microfabricated tissues for investigating traction forces involved in cell migration and tissue morphogenesis. Cell Mol Life Sci. 2017 May 1;74(10):1819–34.

47. Hersen P, Ladoux B. Push it, pull it. Nature. 2011 Feb;470(7334):340–1.

48. du Roure O, Saez A, Buguin A, Austin RH, Chavrier P, Silberzan P, et al. Force mapping in epithelial cell migration. Proc Natl Acad Sci U S A. 2005 Feb 15;102(7):2390–5.

49. Harris AK, Stopak D, Wild P. Fibroblast traction as a mechanism for collagen morphogenesis. Nature. 1981 Mar 19;290(5803):249–51.

50. Mierke CT, Rösel D, Fabry B, Brábek J. Contractile forces in tumor cell migration. Eur J Cell Biol. 2008 Sep 4;87(8):669–76.

51. Rösel D, Brábek J, Tolde O, Mierke CT, Zitterbart DP, Raupach C, et al. Up-Regulation of Rho/ROCK Signaling in Sarcoma Cells Drives Invasion and Increased Generation of Protrusive Forces. Mol Cancer Res. 2008 Sep 1;6(9):1410–20.

52. Li B, Wang JH-C. Fibroblasts and myofibroblasts in wound healing: Force generation and measurement. J Tissue Viability. 2011 Nov 1;20(4):108–20.

53. Kraning-Rush CM, Califano JP, Reinhart-King CA. Cellular Traction Stresses Increase with Increasing Metastatic Potential. PLoS ONE [Internet]. 2012 Feb 28 [cited 2020 Apr 5];7(2). Available from: https://www.ncbi.nlm.nih.gov/pmc/articles/PMC3289668/

54. Dembo M, Wang Y-L. Stresses at the Cell-to-Substrate Interface during Locomotion of Fibroblasts. Biophys J. 1999 Apr 1;76(4):2307–16.

55. Butler JP, Tolić-Nørrelykke IM, Fabry B, Fredberg JJ. Traction fields, moments, and strain energy that cells exert on their surroundings. Am J Physiol-Cell Physiol. 2002 Mar 1;282(3):C595–605.

56. Sabass B, Gardel ML, Waterman CM, Schwarz US. High Resolution Traction Force Microscopy Based on Experimental and Computational Advances. Biophys J. 2008 Jan 1;94(1):207–20.

57. Stricker J, Sabass B, Schwarz US, Gardel ML. Optimization of traction force microscopy for micron-sized focal adhesions. J Phys Condens Matter. 2010 Apr;22(19):194104.

58. Martiel J-L, Leal A, Kurzawa L, Balland M, Wang I, Vignaud T, et al. Chapter 15 - Measurement of cell traction forces with ImageJ. In: Paluch EK, editor. Methods in Cell Biology [Internet]. Academic Press; 2015 [cited 2018 Nov 2]. p. 269–87. (Biophysical Methods in Cell Biology; vol. 125). Available from: http://www.sciencedirect.com/science/article/pii/S0091679X14000090

59. Aratyn-Schaus Y, Oakes PW, Stricker J, Winter SP, Gardel ML. Preparation of Complaint Matrices for Quantifying Cellular Contraction. JoVE J Vis Exp. 2010 Dec 14;(46):e2173.

60. Pakshir P, Alizadehgiashi M, Wong B, Coelho NM, Chen X, Gong Z, et al. Dynamic fibroblast contractions attract remote macrophages in fibrillar collagen matrix. Nat Commun. 2019 Apr 23;10(1):1–17.

61. Chandrasekaran A, Kouthouridis S, Lee W, Lin N, Ma Z, Turner MJ, et al. Magnetic microboats for floating, stiffness tunable, air–liquid interface epithelial cultures. Lab Chip. 2019 Aug 20;19(17):2786–98.

62. Knapp DM, Barocas VH, Moon AG, Yoo K, Petzold LR, Tranquillo RT. Rheology of reconstituted type I collagen gel in confined compression. J Rheol. 1997 Sep 1;41(5):971–93.

63. Yang Y, Kaufman LJ. Rheology and Confocal Reflectance Microscopy as Probes of Mechanical Properties and Structure during Collagen and Collagen/Hyaluronan Self-Assembly. Biophys J. 2009 Feb 18;96(4):1566–85.

64. Arevalo RC, Urbach JS, Blair DL. Size-Dependent Rheology of Type-I Collagen Networks. Biophys J. 2010 Oct 20;99(8):L65–7.

65. Rape AD, Guo W, Wang Y. The regulation of traction force in relation to cell shape and focal adhesions. Biomaterials. 2011 Mar 1;32(8):2043–51.

66. Tseng Q, Duchemin-Pelletier E, Deshiere A, Balland M, Guillou H, Filhol O, et al. Spatial organization of the extracellular matrix regulates cell–cell junction positioning. Proc Natl Acad Sci. 2012 Jan 31;109(5):1506–11.

67. Kovari DT, Wei W, Chang P, Toro J-S, Beach RF, Chambers D, et al. Frustrated Phagocytic Spreading of J774A-1 Macrophages Ends in Myosin II-Dependent Contraction. Biophys J. 2016 Dec 20;111(12):2698–710.

68. Califano JP, Reinhart-King CA. Substrate Stiffness and Cell Area Predict Cellular Traction Stresses in Single Cells and Cells in Contact. Cell Mol Bioeng. 2010 Mar 1;3(1):68–75.

69. Bonnier F, Meade AD, Merzha S, Knief P, Bhattacharya K, Lyng FM, et al. Three dimensional collagen gels as a cell culture matrix for the study of live cells by Raman spectroscopy. Analyst. 2010 Jun 21;135(7):1697–703.

70. Bonnier F, Knief P, Lim B, Meade AD, Dorney J, Bhattacharya K, et al. Imaging live cells grown on a three dimensional collagen matrix using Raman microspectroscopy. Analyst. 2010 Nov 15;135(12):3169–77.

71. Pelham RJ, Wang Y. High Resolution Detection of Mechanical Forces Exerted by Locomoting Fibroblasts on the Substrate. Mol Biol Cell. 1999 Apr 1;10(4):935–45.

72. Munevar S, Wang Y, Dembo M. Traction Force Microscopy of Migrating Normal and H-ras Transformed 3T3 Fibroblasts. Biophys J. 2001 Apr 1;80(4):1744–57.

73. Wice B, Menton D, Geuze H, Schwartz AL. Modulators of cyclic AMP metabolism induce syncytiotrophoblast formation in vitro. Exp Cell Res. 1990 Feb 1;186(2):306–16.

74. Ma Z, Sagrillo-Fagundes L, Tran R, Parameshwar PK, Kalashnikov N, Vaillancourt C, et al. Biomimetic Micropatterned Adhesive Surfaces To Mechanobiologically Regulate Placental Trophoblast Fusion. ACS Appl Mater Interfaces. 2019 Dec 26;11(51):47810–21.

75. Park J, Wysocki RW, Amoozgar Z, Maiorino L, Fein MR, Jorns J, et al. Cancer cells induce metastasis-supporting neutrophil extracellular DNA traps. Sci Transl Med. 2016 Oct 19;8(361):361ra138-361ra138.

76. Lee W, Kalashnikov N, Mok S, Halaoui R, Kuzmin E, Putnam AJ, et al. Dispersible hydrogel force sensors reveal patterns of solid mechanical stress in multicellular spheroid cultures. Nat Commun. 2019 Jan 11;10(1):1–14.

77. Monte Carlo Error Propagation - File Exchange - MATLAB Central [Internet]. [cited 2020 Apr 4]. Available from: https://www.mathworks.com/matlabcentral/fileexchange/57672

78. Mohagheghian E, Luo J, Chen J, Chaudhary G, Chen J, Sun J, et al. Quantifying compressive forces between living cell layers and within tissues using elastic round microgels. Nat Commun. 2018 May 14;9(1):1–14.

79. Vorselen D, Wang Y, de Jesus MM, Shah PK, Footer MJ, Huse M, et al. Microparticle traction force microscopy reveals subcellular force exertion patterns in immune cell–target interactions. Nat Commun. 2020 Jan 7;11(1):1–14.

80. Kaytanlı B, Khankhel AH, Cohen N, Valentine MT. Rapid analysis of cell-generated forces within a multicellular aggregate using microsphere-based traction force microscopy. Soft Matter [Internet]. 2020 Apr 8 [cited 2020 May 2]; Available from: https://pubs.rsc.org/en/content/articlelanding/2020/sm/c9sm02377a

81. Mironov V, Visconti RP, Kasyanov V, Forgacs G, Drake CJ, Markwald RR. Organ printing: Tissue spheroids as building blocks. Biomaterials. 2009 Apr 1;30(12):2164–74.

82. Burdett E, Kasper FK, Mikos AG, Ludwig JA. Engineering Tumors: A Tissue Engineering Perspective in Cancer Biology. Tissue Eng Part B Rev. 2010 Jan 21;16(3):351–9.

83. LaBarbera DV, Reid BG, Yoo BH. The multicellular tumor spheroid model for high-throughput cancer drug discovery. Expert Opin Drug Discov. 2012 Sep 1;7(9):819–30.

84. Stylianopoulos T, Martin JD, Chauhan VP, Jain SR, Diop-Frimpong B, Bardeesy N, et al. Causes, consequences, and remedies for growth-induced solid stress in murine and human tumors. Proc Natl Acad Sci U S A. 2012 Sep 18;109(38):15101–8.

85. Stylianopoulos T, Martin JD, Snuderl M, Mpekris F, Jain SR, Jain RK. Co-evolution of solid stress and interstitial fluid pressure in tumors during progression: Implications for vascular collapse. Cancer Res. 2013 Jul 1;73(13):3833–41.

86. Nia HT, Liu H, Seano G, Datta M, Jones D, Rahbari N, et al. Solid stress and elastic energy as measures of tumour mechanopathology. Nat Biomed Eng [Internet]. 2016 [cited 2020 Apr 4];1. Available from: https://www.ncbi.nlm.nih.gov/pmc/articles/PMC5621647/